Journal of Vacuum Science Technology A



# Hard X-ray Photoelectron Spectroscopy of Tunable Oxide Interfaces

Martina Müller,[1, a)] Patrick Lömker,[2, 3] Paul Rosenberger,[1, 4, 5] Mai Hussein Hamed,[6, 7] David N. Mueller,[5] Ronja A. Heinen,[5] Thomas Szyjka,[1, 5] and Lutz Baumgarten[5]

[1)] *Fachbereich Physik, Universität Konstanz, 78457 Konstanz, Germany*
[2)] *Deutsches Elektronen-Synchrotron, Notkestraße 85, 22607 Hamburg, Germany*
[3)] *Department of Physics, Stockholm University, 10691 Stockholm, Sweden*
[4)] *Fakultät Physik, Technische Universität Dortmund, 44221 Dortmund, Germany*
[5)] *Forschungszentrum Jülich GmbH, Peter Grünberg Institut (PGI-6), 52425 Jülich, Germany*
[6)] *Jülich Centre for Neutron Science (JCNS-2) and Peter Grünberg Institut (PGI-4), JARA-FIT, Forschungszentrum Jülich GmbH, 52425 Jülich, Germany*
[7)] *Faculty of Science, Helwan University, Cairo, 11795, Egypt*

(Dated: November 19, 2021)

The tunability of the oxygen content in complex oxides and heterostructures has emerged as a key to designing their physical functionalities. Controlling the interface reactivity by redox reactions provides a powerful means to deliberately set distinct oxide phases and emerging properties. We present routes on how to control oxygen-driven redox mechanisms in ultrathin ferro(i)magnetic and ferroelectric oxide films and across oxide interfaces. We address the growth and control of metastable EuO oxide phases, the control of phase transitions of binary Fe oxides by oxygen migration, the in operando determination of $NiFe_2O_4/SrTiO_3$ interface band alignments as well as the role of interfacial oxide exchange in ferroelectric $HfO_2$-based capacitors - uncovered by the unique capabilities of photoelectron spectroscopy and in particular using hard X-rays.

## I. INTRODUCTION

The last decade has witnessed that physical functionalities of ultrathin solid films are not only controlled by their bulk electronic structure but, to a significant extent, by their interfaces[1,2]. In metal oxides, the tunability of the oxygen content represents the crucial degree of freedom, which enables to design material functionalities beyond, e.g., the property portfolio of semiconductors[3]. Whether oxygen ions are present or absent at its related lattice site either be a mandatory prerequisite or detrimental to the properties of oxides and may actually even induce new ones[4]. If metal oxide thin films are joined in a heterostructure, thermodynamic and electrochemical nonequilibrium conditions may drive atom and charge exchange across their contacting interfaces. Interface chemical reactions will occur in the case of oxygen transport; charge transfer is promoted by compensating different contact potentials.

In particular, with regard to reduction-oxidation reactions, the importance of the choice of oxide substrate materials has typically been downplayed. Only lately, the huge potential of this determining factor was received for the design of oxide functionalities via interfacial oxide exchange, such as magnetic or ferroelectric oxides[5,6]. The impact of the presence or absence of oxygen is, however, antagonistic: While oxygen ions are an inevitable part of the complex exchange mechanisms in magnetic oxides[7] and its absence leads to a degrading of properties, oxygen vacancies have been identified to induce ferroelectricity in dielectric oxides[8]. Here, a well-balanced presence of vacancies can stabilize a robust ferroelectric state over thousands of electric field switching cycles[6]. Exploiting the tunability of the oxygen content in the materials themselves and understanding interface formation is a versatile strategy of designing new functional properties through controlled interfacial oxygen exchange.

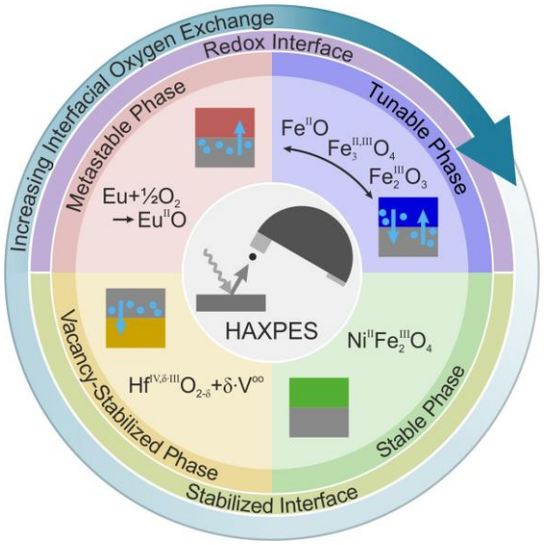


Figure 1. Tunability of complex oxides heterostructures by interfacial oxygen exchange. Redox-active oxide interfaces allow for a growth-controlled stabilization of metastable phases (EuO), or enable even fully reversible phase transitions ($Fe_3O_4$). Thermodynamically less active interfaces, in contrary, can promote vacancy-stabilized phases ($HfO_2$) or interfaces with negligible oxygen exchange ($NiFe_2O_4$).

[a)] Electronic mail:
**Corresponding author:** martina.mueller@uni.kn

X-ray photoelectron spectroscopy (XPS) has been developed as one of the most powerful tools to explore the chemical composition and electronic structure of solids[9,10]. While the probing depth of XPS using laboratory x-ray sources is well suited for studying the subsurface region of an ultrathin film (about 3–5 nm), the photoelectron information depth is significantly enhanced to about 20 –30 nm by performing spectroscopy in the hard X-ray regime (HAXPES)[11]. The strongly reduced photoelectron cross sections at high photon energies are compensated by high brilliance beamlines optimized for HAXPES. Hence the combination of soft- and hard X-ray photoelectron spectroscopy provides the opportunity to element-selectively monitor the redox-driven chemical states, electronic and electrostatic properties of oxide thin films, heterostructures, and buried interfaces.

HAXPES moreover allows for a non-destructive depth profiling by varying either the photon excitation energy or photoelectron emission angle[9]. A quantification of stoichiometry via chemical binding energy shifts is possible down to a few percent, which permits uncovering redox processes by valence changes of oxide phases[12]. The spectroscopic signatures of oxygen vacancies are of indirect nature though and only become apparent by rigid binding energy shifts of core levels, which are caused by changes of the Fermi level position in an altered local electric potential. This approach is also used in the so-called Kraut method, which is successfully applied to derive the band alignment at metal oxide/semiconductor interfaces, provided that there are no chemical reactions[13]. For such samples, the variant of in operando HAXPES becomes applicable, which serves as a powerful tool to determine the band alignment and the chemical state of (oxide) interfaces under operation conditions of an electric device in a single measurement.

This article highlights research examples for which laboratory- and synchrotron-based photoelectron spectroscopy emerged as the key experimental probe to uncover complex oxygen exchange mechanisms in oxide ultrathin films and at oxide interfaces, as schematically depicted in Fig. 1. In particular, emerging interface states and their tunability in ferro(i)magnetic and ferroelectric oxide heterostructures – covering both fundamental aspects and exploring application-relevant devices - are discussed.

## II. REDOX-ASSISTED GROWTH AT METASTABLE OXIDE INTERFACES

In this first section, we present selected examples of how laboratory- and synchrotron-based XPS enables stabilizing the physically exceptionally versatile though metastable Europium Monoxide as ultrathin films in all-oxide heterostructures. EuO is a prototype Heisenberg ferromagnet with a spin-only magnetic moment of $S$ = 7/2 and semiconducting properties[7]. This rare combination has lead to numerous past and recent works on the fundamental spin-dependent electronic properties[14 – 16]. In particular, interfacing EuO to oxides and metals gives rise to emerging quantum states, which origin either from atomic-scale interface growth control or are induced by proximity effects at well-defined interfaces. Recent examples include the emergence of two-dimensional electron systems[17,18], interfacial spin-charge conversion[19] or induced ferroelectric states[20].

Although being particularly prominent as Heisenberg model system, the growth of EuO single-crystalline and ultrathin films is exceptionally challenging because $Eu^{2+}O$ is the metastable suboxide of europium – in contrast to its stable but paramagnetic counterpart $Eu_2^{3+}O_3$. Both a meticulous control over the oxygen backpressure during Eu deposition and the finding that small excesses of Eu metal on hot substrate surfaces are tolerable have enabled the so-called ”distillation” growth of stoichiometric EuO on inert substrates[21]. Not surprisingly, growing EuO on oxide substrates further complicates the synthesis because the interface also needs to be taken into account as a potential oxygen source or sink. Hence, the oxygen-related interface thermodynamics and kinetics strongly determine the EuO film and interface properties as a direct consequence of the growth process[22]. To gain a fundamental understanding of the growth-dependent evolution of this metastable oxide interface, the proceeding EuO deposition process and growth-related interface formation is tracked by in situ XPS.

### A. EuO/YSZ: A quasi-inert ”model” interface?

EuO on yttria-stabilized zirconia (YSZ) is typically regarded as a model system because YSZ (001) and EuO (001) are lattice-matched, and the interface is usually assumed to be quasi-inert, which should result in a both, structurally, and chemically well-defined film/substrate interface[21]. This assumption is corroborated by a thermodynamic Ellingham analysis, which is, however, strictly valid for bulk-like systems only[23].

Here, we focus on the regime of ultrathin EuO films with thicknesses of few monolayers deposited by molecular beam epitaxy (MBE). By using in situ lab-based XPS (Al $K_\alpha$), we probe the stoichiometry of the first monolayers of EuO at the EuO/YSZ interface. Without adding any additional oxygen gas, the Eu metal deposition duration was varied between one and 40 minutes at a substrate temperature $T_S$ = 400 °C. We developed a lab-based strategy for non-destructive depth profiling, i.e., monolayer-controlled Eu deposition is performed stepwise and alternated with in situ XPS analysis.

The corresponding Eu $3d_{5/2}$ spectra for one, two, five, and 40 minutes of Eu deposition are shown in Figure 2 (a). For 1 and 2 min, we find a significant ratio of $Eu^{3+}$ contributing to the spectrum. After five minutes, the $Eu^{3+}$ ratio is drastically reduced but still clearly observable, while after 40 minutes, the spectrum shows a

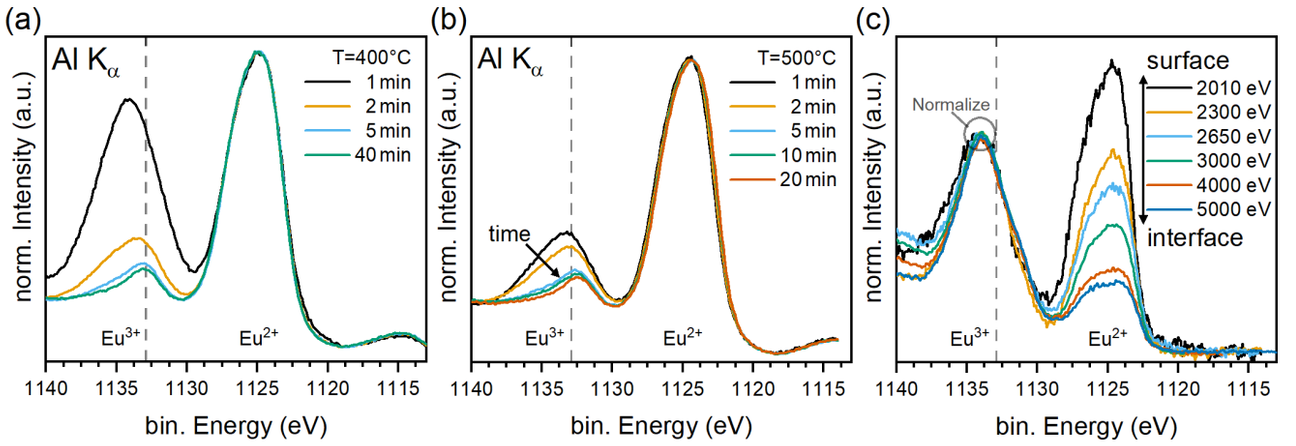


Figure 2. (a) XPS of the Eu $3d_{5/2}$ core level of EuO/YSZ films synthesized by depositing metal only for several deposition times. (b) Lab depth-resolved XPS of an EuO/$SrTiO_3$ bi-layer. (c) Depth profile of a buffered oxide interface system obtained using HAXPES at KMC-1 (BESSY-II). The content of $Eu^{2+}$ increases towards the surface, this is caused by a combination of oxygen mobility and thermodynamic potential through the complex YSZ/ITO interface.

pure $Eu^{2+}$ signal.

Observing $Eu^{3+}$ in the initial phase of the growth process indicates the unexpected formation of $Eu_3O_4$ or $Eu_2O_3$ at the EuO/YSZ interface - which is typically glossed over. Obviously, the thermodynamic landscape of the YSZ interface favours a formation of oxygen vacancies, which on the other hand supplies oxygen to the deposited EuO film[24]. This finding clearly demonstrates that indeed a limited oxygen supply is provided by the YSZ template, which oxidizes EuO to $Eu_3O_4$ or $Eu_2O_3$ – thereby bypassing the thermodynamical prediction for chemically stable bulk EuO/YSZ[23]. Overcoming this phenomenon by e.g. adopted growth parameters allows for synthesizing ultrathin EuO films by depositing Eu metal *even without* externally supplied oxygen on YSZ. Such "redox-assisted" growth may enable to stabilize otherwise metastable oxide interfaces in a straightforward and well-controllable manner. Depending on the specific oxygen ion conductivity of the oxide substrate, also the film thickness becomes well-adjustable by this redox-assisted growth process, as will be discussed in the following.

### B. EuO/$SrTiO_3$: The well-controllable redox interface

Using the previously acquired knowledge on the EuO/YSZ interface, we extend our study to the well-known "work-horse" of oxide electronics, $SrTiO_3$ (STO). Applying the thermodynamical Ellingham analysis, we learn that $SrTiO_3$, and EuO shall *not* coexist and that we ought to expect $Eu_2O_3$ formation. In order to track the oxygen supply at the EuO/$SrTiO_3$ interface, we deposited Eu metal at $T = 500°C$ stepwise on $SrTiO_3$ (001) and performed in situ XPS after each deposition step.

Contrary to the thermodynamic prediction, we observe Eu $3d_{5/2}$ spectra dominated by the $Eu^{2+}$ valence, which is associated with EuO in Figure 2 (b). Indeed, only the first interfacial layer forms as $Eu_2O_3$. For consecutive growth of further layers, the oxygen supply obviously is sufficiently limited, which enables an epitaxial growth of stoichiometric EuO on $SrTiO_3$.

We argue that this mechanism is due to the limited oxygen mobility of the interface – once an initial layer of $Eu_2O_3$ rich phase is formed. This ultrathin intralayer seems to effectively hinder the oxygen supply from the $SrTiO_3$ substrate. The oxygen conductivity of the $SrTiO_3$ substrate is, however, strongly depending on temperature: At room temperature, $SrTiO_3$ shows very limited oxygen mobility, as the EuO/STO interface forms a two-dimensional electron gas (2DEG) as a result of the local oxygen depletion from $SrTiO_3$ to EuO[17]. Performing higher temperature studies (at and above 700 °C), we were able to show that only highly oxidized $Eu_2O_3$ forms. Obviously, the oxygen mobility now exceeds a critical value, and both film and $SrTiO_3$ serve as a permanent source of oxygen for EuO oxidation. This tunability of interfacial oxygen supply enables performing oxide on oxide growth of two reactive oxides in a well-defined temperature range.

This finding underlines the importance of the oxygen mobility of film and substrate as active parts of the growth process. Here, we find a temperature-dependent growth window to perform oxide-on-oxide growth of the otherwise reactive oxides EuO and $SrTiO_3$. The interface may even be used to functionalize the system as 2DEG or as a tunnel barrier, dependent on the type of oxygen vacancies forming in $SrTiO_3$ by the redox process at low temperatures without oxygen replenishing. On the methodical side, the alternating Eu deposition and XPS analysis enable an extensive pre-characterization prior to synchrotron measurements, e.g., unveiling aforementioned two-dimensional electron gas. Moreover, it high-

lights the usefulness of a combined lab XPS/MBE infrastructure for the characterization of challenging synthesis of metastable oxide-on-oxide materials.

### C. EuO/ITO: An instable oxygen source and sink

What happens eventually if metastable EuO is to be stabilized on an oxide template which itself is a very good oxygen ion conductor? A suitable substrate to investigate this aspect is ITO/YSZ, i.e., a "virtual substrate" for which an indium tin oxide (ITO) layer is grown sufficiently thick on lattice-matched YSZ (001) such that the YSZ substrate can be disregarded. The growth is performed by reactive MBE at 400 °C using a Eu flux rate of 0.13 Å $s^{-1}$ and an oxygen partial pressure of $1.7 \times 10^{-7}$ mbar. A 10 nm Al capping is applied after growth to prevent further oxidation.

In order to enable a non-destructive chemical depth-profiling of the EuO film and interface, we here employ hard X-ray photoelectron spectroscopy using variable synchrotron radiation. The HAXPES experiments were conducted at the KMC-1 beamline at BESSY II (Berlin) with the HIKE endstation[25]. We vary the inelastic mean free path $\lambda$ of the emitted photoelectrons as function of the photon energy between 3 nm (2010 eV) and 9 nm (5000 eV)[26].

The results are shown in Figure 2 (c). We study the Eu $3d_{5/2}$ core-level and normalize the data to the binding energy of $Eu^{3+}$. In doing so, we observe a chemical gradient with a small content of $Eu^{2+}$ at the interface, which increases towards the surface. Using established models[27] we identify this as a mixed- or bilayer system with 1.2 nm of EuO and the rest of the nominally 4 nm layer consisting of $Eu_2O_3$. The thermodynamic Ellingham analysis clearly reveals that EuO on ITO is an unstable phase, unlike YSZ, which is expected to be compatible with EuO growth. We note that at these temperatures, oxygen is extremely mobile in ITO; for samples grown at room temperature, fully reduced In metal is observed at the substrate's surface (not shown). In this way, HAXPES enables non-destructive chemical depth profiling by varying the probing depth across interfaces and quantifying the different chemical states of the exemplarily highly reactive EuO/ITO interface.

### D. Opportunities of redox-assisted oxide growth

The interface-sensitive studies performed by lab XPS and HAXPES show that even on commonly used model substrates like YSZ, which is, e.g., regarded as inert with respect to the formation of $Eu^{3+}$, interfacial redox processes have to be taken into account. Figure 3 summarizes the acquired results, contrasting in (a) the thermodynamical expectations with (b) the spectroscopically acquired results on interface formation of ultrathin film

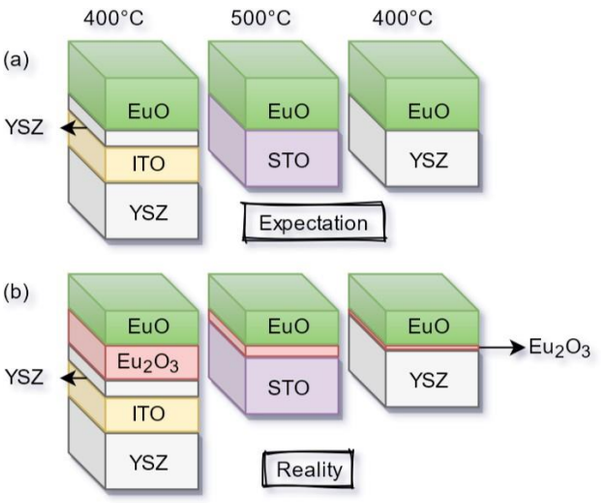


Figure 3. Schematic depiction comparing the (a) thermodynamic expectation and (b) the experimental findings for interface formation of ultrathin film deposition of EuO on oxidic substrates, i.e., ITO, $SrTiO_3$, and YSZ.

deposition of EuO on (001)-oriented ITO, STO and YSZ substrates, respectively.

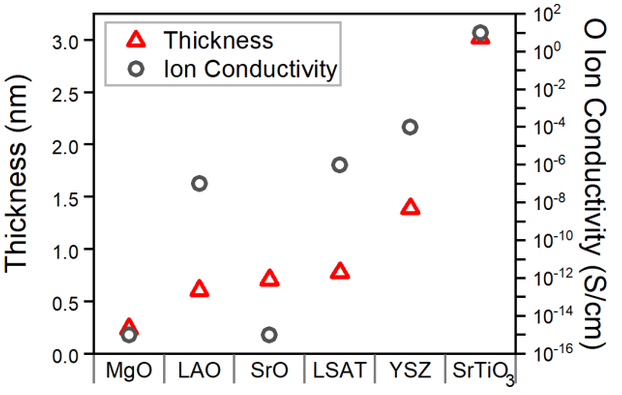


Figure 4. Correlation of oxygen ion conductivity of selected oxide substrates and redox-grown Eu oxide film thicknesses.

Redox-driven interface reactions need to be considered for stabilizing EuO or other metastable materials on any oxide substrate. As summarized in Figure 4, we performed a study on the growth of EuO onto different oxide substrates, i.e. SrO (5 nm on $SrTiO_3$), YSZ, LAO, MgO, and LSAT. We find that the substrate's oxygen ion conductivity correlates well with the film thickness after 5 min of Eu deposition. We could show that the Eu distillation condition can be fulfilled on all of these oxides, rendering them eligible for a kinetic (external) oxygen-free growth mode as described for $SrTiO_3$[28].

This interface-sensitive study performed by lab XPS shows that even on the commonly used model substrate

YSZ, which is regarded as inert with respect to the formation of $Eu^{3+}$, interfacial redox processes have to be taken into account. This circumstance has to be considered for growing EuO or other metastable materials on any oxide substrate and may even be used as a route to stabilizing oxide phases otherwise not accessible by the standard phase diagram.

## III. THERMAL PHASE CONTROL OF OXIDE INTERFACES

Albeit being a classical - if not the most ancient - magnetic material, current research on iron oxide $Fe_xO_y$ thin films actively continues developing due to its applications in a broad range of fundamental and technological fields[3]. Functional properties of binary iron oxides thereby range from insulators to conductors and from ferromagnets to antiferromagnets[7]. The prospect of a controlled interconversion between different iron oxide phases, and hence, the deliberate setting of magnetic and/or electrical properties, may open up novel possibilities in oxide electronics. One route towards such tailored reduction-oxidation reactions is by employing an oxide substrate as a - thermally controllable - source or sink of oxygen.

In the following, we will discuss mechanisms that enforce the reduction of magnetite $Fe_3O_4$ thin films towards lower oxidations states and finally towards Fe metal. Using the depth- and elemental sensitivity of HAXPES allows us to explore the thermally induced chemical transitions between different phases of iron oxide thin films. The information depth for samples illuminated by hard X-rays at a photon energy of 4 keV is approximately 20–25 nm, which enables to capture spectroscopic information from the bulk as well as the buried oxide interfaces. All data presented in this chapter was recorded at the HIKE beamline at BESSY II (HZB Berlin, Germany) using a photon energy of 4 keV[25].

To introduce the relevant material properties, magnetite $Fe_3O_4$ crystallizes in an inverse spinel structure with $Fe^{3+}$ occupying the octahedral site, whereas the tetrahedral sites are comprised of a mixture of $Fe^{2+}$ and $Fe^{3+}$ cations. The structure orders magnetically at a Curie temperature of $T_C$ = 860 K. $Fe_3O_4$ has half-metallic conducting properties and undergoes a metal-to-insulator ("Verwey") transition at $T_V$ = 120 K, which is recognized as a sensitive fingerprint for the $Fe_3O_4$ phase stoichiometry. Details on the growth of $Fe_3O_4$ films on $SrTiO_3$(001) and YSZ(001) substrates by pulsed laser deposition (PLD), as well as their throughout structural and magnetic characterization have been published elsewhere.[29–31].

### A. As-prepared $Fe_3O_4$/STO: The unexpected interface

The first challenge is to conclude on the stoichiometry of as-grown $Fe_3O_4$ thin films. Here, the Verwey transition can serve as a very sensitive signature of the $Fe_{3-\delta}O_4$ phase because it can only be detected for $\delta < 0.045$[32]. This upper oxygen detection limit may even be more sensitive than a quantitative stoichiometry analysis by XPS or HAXPES, for which the elemental sensitivity is typically in the order of 1% depending on specific core-level cross-section and peak intensity. We note that besides the oxygen content itself, also the structural phase, lattice strain, and domain size can alter the Verwey transition temperature of $Fe_{3-\delta}O_4$. However, we recently demonstrated that the $Fe_3O_4$ thin films grow structurally fully relaxed[33,34]. This is why we can directly relate the observation of the Verwey transition to the upper oxygen content, which serves as an alternative measure in addition to HAXPES data.

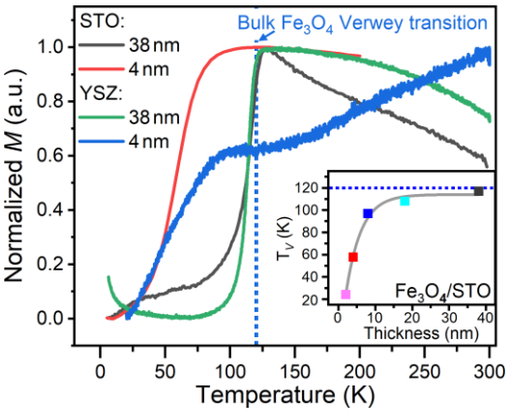


Figure 5. Magnetization vs. temperature $M(T)$ curves to detect Verwey transition of 38 nm and 4 nm $Fe_3O_4$ thin films grown on YSZ and $SrTiO_3$ substrates, respectively. (Inset) Verwey transition temperature $T_V$ as a function of film thickness for $Fe_3O_4$ grown on $SrTiO_3$.

The Verwey transition was recorded for $Fe_3O_4$ thin films grown on YSZ and $SrTiO_3$ with thicknesses of 38 nm and 4 nm via magnetization vs. temperature $M(T)$ curves, as shown in Figure 5. Below $T_V$ , $Fe_3O_4$ transfers from a cubic to a monoclinic structure which causes a decrease of the magnetization. The magnetization as a function of temperature $M(T)$ of the 38 nm films grown on both YSZ and $SrTiO_3$ drops around 120 K which is corresponding to the Verwey transition. This observation suggests a bulk-like stoichiometry of the 38 nm $Fe_3O_4$ films grown on both $SrTiO_3$ and YSZ.

For an ultrathin film of 4 nm thickness grown on YSZ and $SrTiO_3$, the Verwey transition is still detectable but decreases to 60 K, as shown in the inset of Figure 5. While its detectability indicates a high structural and stoichiometric quality of the $Fe_3O_4$ films, the reduced $T_V$ points towards its reduced dimensionality. Indeed, by HAXPES analysis of the Fe 2p spectra, we can extract the formation of a 2 u.c. of $\gamma$-$Fe_2O_3$ intralayer between $Fe_3O_4$ and the substrates[29,30], which reduces the effective $Fe_3O_4$ thickness. From a thermodynamic perspective, this finding is unexpected as no driving force for further oxidation

of the $Fe_3O_4$ shall exist according to an Ellingham analysis - at least for bulk $Fe_3O_4$ and substrates. Once more, we find an oxide interface behaving opposite to theoretical predictions - which in turn opens up novel possibilities for its thermal tunability via the substrate's oxygen supply, which we explore in the following.

### B. Tuning iron oxide phases by post-annealing

To record the thermally induced phase transition from $Fe_3O_4$, HAXPES experiment on the above samples were conducted in the following manner: Fe 2p core-level spectra were recorded during stepwise post-annealing of the samples between temperatures of 25-700 °C in UHV, and each step was stabilized for 20 min. Moreover, to test whether the Fe 2p spectra are recorded at quasi-equilibrium, a film of 4 nm was annealed at 600 °C for 90 min and HAXPES Fe 2p was recorded every 30 min. No changes in peak position or -shape appear in the spectra.

Figure 6 (a) depicts Fe 2p core-level spectra of the as-grown $Fe_3O_4$ films. To identify the Fe valency, the experimental spectra were compared to reference data of FeO[35], $Fe_2O_3$, and $Fe_3O_4$[36]. The emergence and position of satellite peaks yield clear indication for the presence of $Fe^{3+}$ and/or $Fe^{2+}$, see Figure 6 (a). The satellite peaks of FeO and $Fe_2O_3$ phases have binding energies $E_B$ of 715.5 eV and 719 eV, respectively. On the other hand, the satellite peaks of $Fe_3O_4$, which has a mixed oxidation state of $Fe^{2+}$ and $Fe^{3+}$, merge and thus disappear, as apparent for the 38 nm film grown on $SrTiO_3$ substrate in Figure 6 (a). For 38 nm thick $Fe_3O_4$, consequently, we find that the two satellites are merged. Moreover, the Fe $2p_{3/2}$ core level is composed of the $Fe^{3+}$ peak and a shoulder that refers to $Fe^{2+}$. We conclude on a bulk-like stoichiometry of 38 nm thick $Fe_3O_4$ films. For 4nm films grown on $SrTiO_3$ and YSZ substrates, we observe that the $Fe^{3+}$ satellite peak appears accompanied by a decrease $Fe^{2+}$ peak shoulder at the Fe $2p_{3/2}$ peak. Both observations suggest the formation of an interfacial $Fe_2O_3$ phase in addition to $Fe_3O_4$.

For films annealed at $T_{anneal}$ = 400 °C in UHV-atmosphere, as shown in Figure 6 (b), the films with thicknesses of 4 nm and 38 nm grown on STO substrates show the appearance of a satellite peak at $E_B$ = 715.5 eV, which indicates the formation of a FeO and partial $Fe_3O_4$ phase. However, for film grown on YSZ, the satellite peak intensity at $E_B$ = 715.5 eV is stronger and indicates the full reduction to FeO. On the other hand, for films annealed at $T_{anneal}$ = 700 °C in UHV-atmosphere as shown in Figure 6 (c), the 38 nm film grown on STO shows a partial reduction to FeO, whereas the 4 nm film grown on STO shows a full reduction to FeO indicated by the intensities of the satellite peaks. Surprisingly, the 4 nm thick film grown on YSZ is fully reduced to Fe metal.

### C. Beyond the standard phase diagram: A thermodynamic discussion

The previous results unveil the strong differences between YSZ and STO substrates in their affinity to be chemically reduced. However, the formation of interfacial $\gamma$-$Fe_2O_3$ is observed for both systems, $Fe_3O_4$/STO and $Fe_3O_4$/YSZ. Figure 7 summarizes the resulting heterosystem before and after annealing. The mechanism for the formation of the interfacial $\gamma$-$Fe_2O_3$ phase between $Fe_3O_4$ films and STO and YSZ substrates remains to be discussed.

Taking into account the thermodynamic properties of all constituents, $SrTiO_3$ has a lower Gibbs free energy of formation $\Delta G^o_F = -1588.4$ kJ/mol compared to $Fe_3O_4$ ($\Delta G^o_F = -1015.4$ kJ/mol). Therefore, STO is not expected to oxidize $Fe_3O_4$. However, oxygen vacancies perturb the formation energy for $TiO_2$-terminated STO to 461.5 kJ/mol.

Consequently, the formation of an oxidized $\gamma$-$Fe_2O_3$ intralayer may be explained by the oxygen diffusion from the STO substrate due to the reduced surface formation energy by oxygen vacancies of $TiO_2$-terminated STO surfaces, which enables the migration of oxygen from STO into $Fe_3O_4$. We note that this mechanism may simultaneously lead to the formation of reduced $Ti^{3+}$ at the STO interface, which is the key prerequisite for the formation of a redox 2DES[17].

From bulk thermodynamics, the formation enthalpies of $Fe_3O_4$ and YSZ have similar values. Therefore, no clear expectation of which phase may reduce the other can be drawn. It should be noted, however, that since YSZ is such a good oxygen ion conductor, any formation of additional oxygen vacancies (concomitant with reduction of Zr) at the interface will be followed by a rapid redistribution, making the concentration of excess oxygen vacancies at the interface quite small.

Additionally, YSZ is known to be a good electrolyte because of its high oxygen conductivity which is influenced by the doping level as well. Therefore, oxygen can diffuse from the outer atmosphere through the YSZ substrate and cause the formation of an $Fe_2O_3$ intralayer. Therefore, the oxygen conductivity of YSZ is a key factor for the formation of an oxidized $Fe_3O_4$ intralayer. However, the perturbation of oxygen vacancy concentration caused by this redistribution within the substrate crystal plays a negligible role.

To conclude, we studied the effect of annealing in different oxygen pressure and the emerging redox processes of $Fe_3O_4$ interfaces. A thermodynamics modeling allows to understand phase transformations between $Fe_3O_4$, $\gamma$-$Fe_2O_3$, and FeO through the oxygen migration across interfaces with oxide substrates $SrTiO_3$ and YSZ. This finding convincingly demonstrates the important role of the oxide substrates STO and YSZ as oxygen scavengers or suppliers. In this way, alternative opportunities emerge to control interface and thin-film functionalities of all-oxide heterostructures.

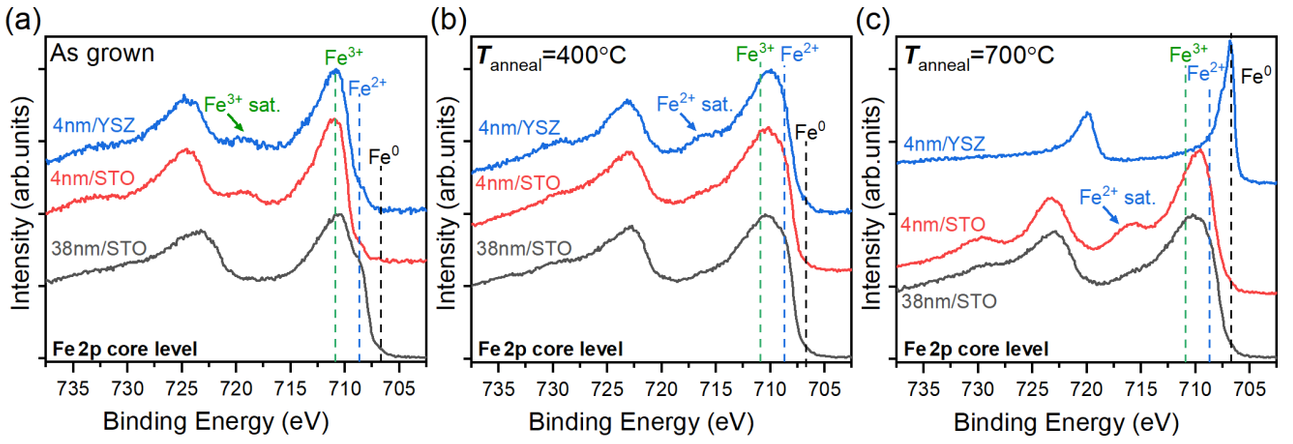


Figure 6. Fe 2p core level spectra recorded for 38 nm and 4 nm $Fe_3O_4$ films grown on $SrTiO_3$ and YSZ. (a) As-grown $Fe_3O_4$ films, (b) $Fe_3O_4$ films annealed at temperatures of $T$ = 400 °C and (c) $T$ = 700 °C in UHV atmosphere, respectively.

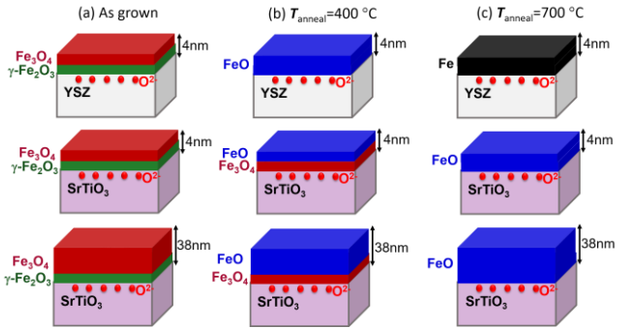


Figure 7. (a) Schematics of as-grown iron oxide heterostructures with thicknesses of $d$ = 4 nm (50 % $\gamma$-$Fe_2O_3$ and 50 % $Fe_3O_4$) on YSZ (top) and Nb:$SrTiO_3$ substrates (middle), respectively, and $d$ = 38 nm on Nb:$SrTiO_3$ (bottom). (b),(c) Same set of samples, but annealed to (b) $T_{anneal}$ = 400 °C and (c) $T_{anneal}$ = 700 °C in UHV-atmosphere.

## IV. BAND ALIGNMENT AT OXIDE INTERFACES

Key parameters of any semiconductor (SC) device are the electronic band alignment and -offsets at the interfaces of a metal-insulator (M/I) heterostructure. HAXPES can serve as an experimental tool to directly extract the valence band (VB) offsets of buried interfaces[11]. In addition, also the interfacial chemical state is accessible, which makes HAXPES a unique tool for a thorough interface characterization[9]. Furthermore, performing HAXPES experiments in operando, i.e., under applied bias voltage, both the band alignment and the chemical state of a M/I device can be determined under realistic operation conditions - and captured in a concurrent measurement[37,38]. In this chapter, we discuss an Au/$NiFe_2O_4$/$SrTiO_3$ heterostrocture as a prototype example for an in operando HAXPES experiment, as schematically sketched in Figure 8.

$NiFe_2O_4$ directly compares to $Fe_3O_4$, as both materials adopt the inverse spinel crystal structure. In $NiFe_2O_4$, divalent Ni cations occupy the $Fe^{2+}$ lattice sites of the $Fe_3O_4$ unit cell. The thereby altered magnetic exchange and electronic correlations turn $NiFe_2O_4$ into an (also) ferrimagnetic but insulating material, with a similar Curie temperature of about 850 K[39]. In Figure 9(b), the $NiFe_2O_4$ spectral signatures of the Fe 2p core level spectra thus shows a $Fe^{3+}$-only feature which lacks the $Fe^{2+}$ shoulder, as observed for $Fe_3O_4$ in Figure 6 (a). With regard to the chemical stability, however, $NiFe_2O_4$ and $Fe_3O_4$ strongly differ: the $NiFe_2O_4$/STO interface turns out to be chemically extremely robust compared to $Fe_3O_4$/STO. No signatures of interfacial redox reactions could be observed by HAXPES for $NiFe_2O_4$[40]. Thus, the $NiFe_2O_4$/STO heterostructure serves as a prototype example for a quasi-nonreactive M/I interface, which in turn is a prerequisite for an in operando HAXPES characterization.

### A. Experimental in operando HAXPES

The design of samples for in operando HAXPES measurements requires metal top electrodes to apply a bias voltage. On the other hand (in order to adapt to the information depth of the HAXPES experiment), these electrodes need to be structured into different regions which either can be electrically contacted (thick metal pad) or can be probed by HAXPES while applying the bias potential (thin metal overlayer).

Figure 8 sketches a possible heterostructure for in operando HAXPES. Half of the Nb-doped $SrTiO_3$ substrate is covered with a 500 $\mu$m $SiO_2$ film which serves as a buffer between the STO back electrode and Au top electrode. On top of STO, a 10 nm $NiFe_2O_4$ layer is deposited via pulsed laser deposition. Next, a 4 nm thin Au pad (2 mm x 3.6 mm) is deposited ex situ via electron beam vapor deposition, which overlaps the $SiO_2$

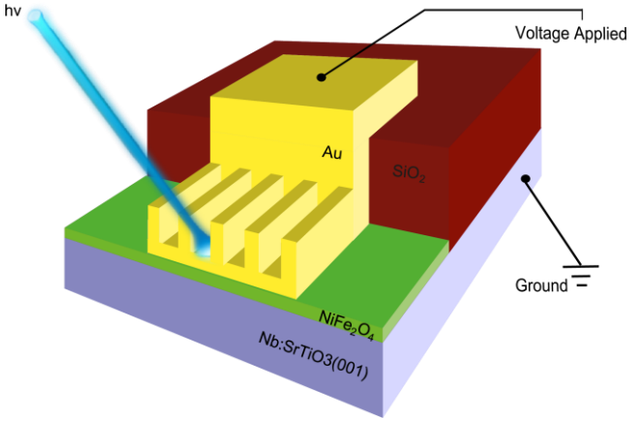


Figure 8. Schematics of an in operando HAXPES measurement on a structured Au/$NiFe_2O_4$/$SrTiO_3$ heterostructure.

and $NiFe_2O_4$/$SrTiO_3$ areas. On top of this thin gold pad, a 40 nm gold finger structure is deposited. The fingers width and distance between the fingers is 0.2 mm, respectively. The top Au electrode is connected to the voltage source and the $SrTiO_3$ substrate is grounded.

In operando HAXPES experiments were performed at beamline P09 (now P22) at PETRA III (DESY Hamburg, Germany)[41] in normal emission geometry using a photon energy of 6 keV. For each voltage step the electrical current was measured, see Figure 9 (a). As reference data, spectra of a $SrTiO_3$ substrate, a 20 nm $NiFe_2O_4$ film and a 50 nm Au film were recorded.

### B. Chemical Stability of the $NiFe_2O_4$/STO Interface

In order to determine the band alignment of the Au/$NiFe_2O_4$/$SrTiO_3$ heterostructure in operando, the layers and interfaces need to be chemically stable – not only thermodynamically, but also under applied bias voltages during the HAXPES measurement[13]. Figure 9 (b) displays the Fe 2*p* core level for varying applied voltages, whereby the on-potential spectra had been shifted on the binding energy (BE) scale on the zero voltage Fe 2*p* position. No spectral changes of the core levels are observed. In particular, at the low binding energy flank of the Fe $2p_{3/2}$ peak, no shoulder of a possibly emerging $Fe^{2+}$ component can be identified, and also the position of the $Fe^{3+}$ satellite peak remains unchanged. Hence, $NiFe_2O_4$ can be assumed to be chemically stable during the in operando HAXPES measurement.

For each voltage step, the electrical current was observed to check whether the sample had not been shorted. A positive applied voltage refers to a direction where negative charges move from the $SrTiO_3$ to the $NiFe_2O_4$, while a negative applied voltage refers to a direction vice versa. The resulting *I-V* curve is shown in figure 9 (a). We find a symmetrical and non-ohmic response indicative of a M/SC/M structure. Although $NiFe_2O_4$ is expected to be insulating, the growth of $NiFe_2O_4$ on $SrTiO_3$ introduces defects like dislocations or mosaicity due to the large lattice strain[39,40]. $NiFe_2O_4$ therefore electrically acts as a semiconductor. In general, throughout the entire in operando HAXPES measurement process, the sample was electrically and chemically stable, as shown in Figures 9 (a) and (b).

### C. Band alignment analysis via HAXPES

In a simple but powerful model used in semiconductor physics, the valence band (VB) offset $\Delta E_v$ at the interface of two SCs *A* and *B* is simply determined by the energy difference of their VB maxima $E_v$, $\Delta E_v = E_v^A - E_v^B$. The same relation holds for the Schottky barrier height $\Phi_B$ of a metal/SC interface, here the metal valence band maximum is given by the Fermi energy, $\Phi = E_F^M - E^{SC}$

In an (oxide) heterostructure, however, the VBs of the different materials are overlapping and thus the VBs of the individual layer often cannot be directly recorded by HAXPES. Therefore, an indirect method is typically applied, which relates a core level binding energy position to the actual position of the valence band. This so-called "Kraut model" assumes flat bands and chemically stable interfaces[13]. If these conditions are fulfilled, it can be used to determine the band alignment and the band offset at the interfaces of (oxide) heterostructures, here Au/$NiFe_2O_4$/$SrTiO_3$.

According to Kraut's model[13], the measured energy difference between any core level peak maximum and the VB maximum of a reference material A is taken as a constant value, also if material A is part of a heterostructure. Thus, binding energy changes of the core level should directly reflect the same changes at the VB maximum.

$$(E_{cl}^A)_{ref} - (E_v^A)_{ref} = (E_{cl}^A)_{het} - (E_v^A)_{het} \qquad (1)$$

Due to the element selectivity of HAXPES, specific core levels can be related to the individual layers of a heterostructure, and hence the VB position of the individual layers can be determined: The experimentally not accessible valence band maximum $(E_v^A)_{het}$ is now substituted by the difference of the equivalent core level binding energies relative to the reference sample.

$$(E_v^A)_{het} = (E_v^A)_{ref} - [(E_{cl}^A)_{ref} - (E_{cl}^A)_{het}] \qquad (2)$$

Now, the VB offset $E_v$ or Schottky barrier height $\Phi_B$ between different materials A and B, here Au/$NiFe_2O_4$ and $NiFe_2O_4$/$SrTiO_3$, becomes experimentally accessible by using equation (2).

For the determination of the band alignment of the Au/$NiFe_2O_4$/$SrTiO_3$ model sample, the core level binding energies of the Au $4f_{7/2}$ level for the Au top electrode, the Fe $2p_{3/2}$ and Ni $2p_{3/2}$ level for the $NiFe_2O_4$,

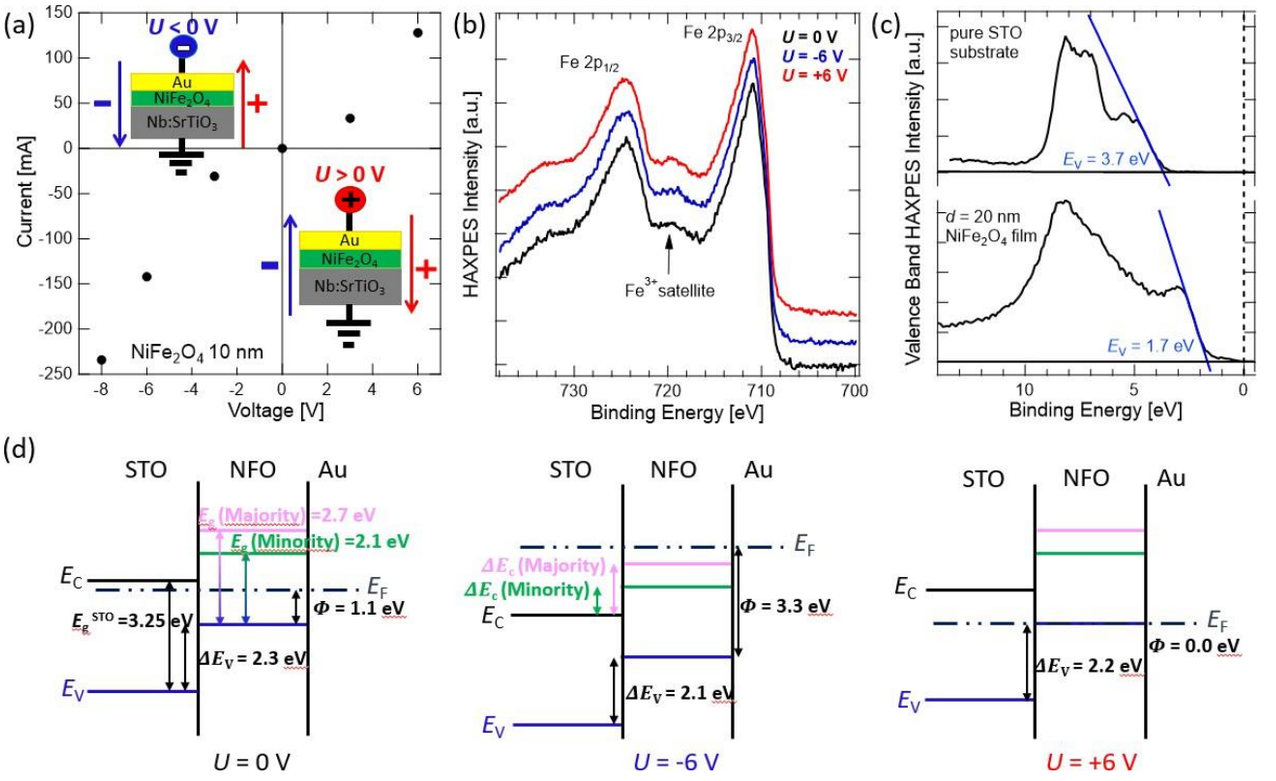


Figure 9. (a) Electric $I$-$V$ curves recorded during in operando HAXPES of a Au/$NiFe_2O_4$/$SrTiO_3$ heterostructure. (b) BE-corrected Fe 2p core levels, for which the on-potential spectra under ± 6 V bias are shifted on top of the 0 V measurement. (c) Determination of the valence band offset of the reference $SrTiO_3$ and $NiFe_2O_4$ samples. (d) Band alignment determined by the Kraut method with respect to the applied voltage.

and the Ti $2p_{3/2}$ and Sr $3d_{5/2}$ level for the $SrTiO_3$ layer are analyzed. As reference samples an uncovered $SrTiO_3$ substrate, a 20 nm $NiFe_2O_4$ film and a 50 nm Au film are used. The Fermi level $E_f$ of Au was used as binding energy reference and set to zero. As depicted in Fig. 9(c), the VB edges $E_v$ of the $SrTiO_3$ and $NiFe_2O_4$ reference samples are determined by fitting[42].

In Figure 9(d), the resulting band alignment is shown. The conduction band positions $E_c$ are calculated by adding the band gap $E_g$ to the VB offsets $\Delta E_v$. For $SrTiO_3$, a band gap of $E_g$=3.25 eV is assumed[43] and for $NiFe_2O_4$ the calculated majority and minority band gaps of $E_g$ =2.7 eV and $E_g$ =2.3 eV are used[44]. The bias dependent band alignments diagrams for $U$ =0 V,6 V,– 6 V of the Au/$NiFe_2O_4$/$SrTiO_3$ heterostructure are shown in figure 9(d), with the corresponding I-V curve depicted in Figure 9(a).

We find the spectroscopically determined $\Delta E_v$ at the $NiFe_2O_4$/$SrTiO_3$ interface being independent of the applied voltage, while $\Phi_B$ at the Au/$NiFe_2O_4$ interface strongly changes. Thus, the electrical transport characteristics of the Au/$NiFe_2O_4$/$SrTiO_3$ heterostructure are mainly governed by the Au/$NiFe_2O_4$ interface. For $U$ =0 V, the Fermi level $E_f$ is located in the band gap of the $NiFe_2O_4$ and close to the conduction band $E_v$ of $SrTiO_3$. Due to its Nb-doping, the $SrTiO_3$ is electrically conducting. For small voltages, the $NiFe_2O_4$ acts as a barrier, and only small currents are expected, which fits well with the observed nonohmic, symmetrical I-V curve in Figure 9(a). At $U$ =− 6 V, the Fermi level $E_f$ is located in the conduction band of the $NiFe_2O_4$ and the $SrTiO_3$. Thus, there is a conducting path established, which is also observed in the I-V curve. In the case of $U$ =6 V, the Fermi level $E_f$ aligns with the valence band edge of $NiFe_2O_4$ and lays in the band gap of $SrTiO_3$. Thus, again a conducting channel is established, which is confirmed by the I-V curve in Figure 9(a).

From the above experiments, an element-specific quantification of band alignments of a complex oxide heterostructure was realized, which confirms the results of electrical $I$-$V$ measurements. In that, in operando HAXPES is a powerful spectroscopic tool to probe multilayer devices under realistic operation conditions.

## V. INTERFACE OXIDE EXCHANGE IN FERROELECTRIC CAPACITORS

The previous sections discussed mechanisms by which controlled oxygen supply by oxide substrates can be uti-

lized to deliberately set ferro(i)magnetic oxide properties of ultrathin films. On the other hand, ferroelectricity in dielectric $HfO_2$-based compounds is mainly introduced by the *absence* of oxygen, introduced either by doping or directly by oxygen vacancies[45]. Ferroelectric (FE) capacitors based on simple metal–FE insulator–metal (MIM) structures are envisioned as efficient nonvolatile memory devices[46]. Since its discovery around 2010, $HfO_2$-based ferroelectric materials, in particular $Hf_{0.5}Zr_{0.5}O_2$ (HZO), emerged as most promising candidates due to their outstanding CMOS compatibility.

In practice, however, performance instabilities such as the so-called wake-up, imprint, and fatigue effects are still poorly controllable and currently hamper its application in commercial FE memory devices[47,48]. The common feature of these issues is the emergence of excess oxygen vacancy defects located within the ferroelectric $HfO_2$-based layer with an increased density at the electrode interfaces. Thus, the control of the oxygen defect density within the $HfO_2$-based layer and at its interfaces is currently of major interest.

It has become evident that the choice of the metallic electrode material in MIM capacitors plays a crucial role, in particular, because the interface chemical state modulates the oxygen exchange across the interface - which can either act passively or rather as a source or sink of oxygen. Hence, the material choice can either increase or reduce the defect density at the $HfO_2$ interface and exploiting the tunability of oxygen vacancy density is a major aspect in current MIM design. HAXPES as an element-selective, depth-sensitive and non-destructive analysis tool serves as an ideal probe for the emerging interface chemistry. All HAXPES data presented in this section had been recorded at the beamline P22 of PETRA III (DESY Hamburg, Germany) using a photon energy of 6 keV[49].

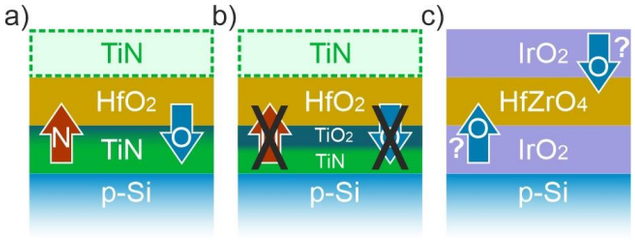


Figure 10. Different interface oxygen exchange mechanisms occur in $HfO_2$-based MIM structures, dependent on the choice of the metal electrodes: (a) oxygen scavenging by a TiN electrode, (b) interface passivation by a $TiO_2$ interlayer, and (c) possible oxygen supply by an $IrO_2$ electrode.

Figure 10 (a)–(c) schematically depicts three MIM structures for which oxygen exchange mechanisms across the interface was explored by HAXPES. Their specific preparation conditions by either physical vapor deposition (PVD)[45] or/and atomic layer deposition (ALD)[50] were taken into account for discussion of the spectroscopic results, as in particular the oxygen supply before or during $HfO_2$ layer growth significantly alters the interface properties. Moreover, all three capacitors devices had been characterized electrically by polarization-voltage (P-V) curves[45,51], and hence a direct relation between the interface chemical properties and ferroelectric state of the MIM structures can be drawn.

### A. Oxygen scavenging by TiN electrodes

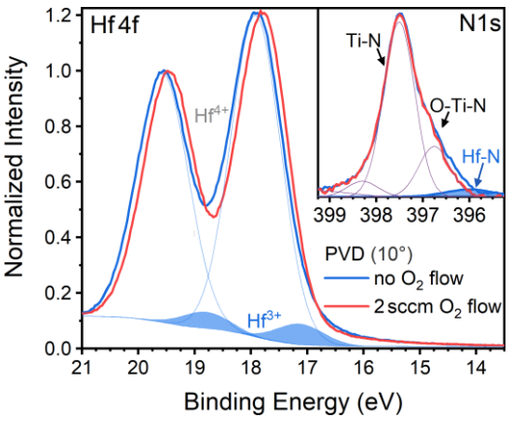


Figure 11. Hf 4f core-level spectra for $TiN/HfO_2/TiN$ capacitors grown at different oxygen ambiences (0 and 2sscm). Without additional oxygen supply, a $Hf^{3+}$ component appears (blue shaded area). The inset shows the related N 1s spectra, for which a HfN component is evident.

For $TiN/HfO_2/TiN$ capacitors, the interface properties strongly depend on the specific PVD growth parameters: Figure 11 depicts the Hf 4f core levels recorded from two samples for which either no or 2 sccm gaseous oxygen was provided before and during $HfO_2$ layer growth. For a direct comparison, the rigid binding energy shift between the two measurements was corrected, and both spectra were subtracted from each other. This differential spectrum (shaded blue area) reveals a double peak structure with the same energy splitting as the Hf 4f doublet, but shifted by 600 meV to lower BE values and with an intensity ratio of about 5% compared to the main Hf 4f doublet. This feature is assigned to a spectral contribution of a $Hf^{3+}$ valency in agreement with literature[52], and its intensity strongly decreases with the amount of supplied oxygen during the growth process as discussed in[53]. We note that the N 2s component, which appears at about 15.5 eV binding energy, can be neglected in the spectral analysis of the Hf 4f level. Compared to Hf 4f and N 1s core levels, the N 2s peak has an about one order of magnitude lower cross section and is covered by a 10 nm $HfO_2$ layer, hence, its intensity is below the detection limit.

For the N 1s core level shown in the inset of fig. 11, we also compared the differential spectra and found an enhanced spectral weight at the lower binding energy side for the sample without additional oxygen supply. This

contribution can be assigned to the presence of HfN[54]. Further, the peak located at $E_B$ = 397.5 eV is assigned to TiN and the peak fit at $E_B$ = 396.7 eV can be related to a $TiN_xO_y$ contributions[55]. In analogy to the Hf 4f spectrum, the formation of the HfN related component is found to decrease the amount of oxygen provided during the growth process[53].

The emergence of $Hf^{3+}$ spectral weight in the Hf 4f core level may either be interpreted as HfN contribution or as an indirect signature of positively single and double-charged oxygen vacancies, $V_O^{\bullet}$ and $V_O^{\bullet\bullet}$. From angular dependent HAXPES measurements (not shown), the $Hf^{3+}$ contribution can be located at the interface between $HfO_2$ and the bottom TiN electrode. As the HfN component is observed in the N 1s core-level spectra, an interfacial HfN formation seems likely. However, oxygen vacancies are also known to be enhanced at the interfaces. Thus both contributions may contribute to the $Hf^{3+}$ component.

At this point, we conclude that without additional oxygen supplied during PVD growth, the TiN electrode can exchange nitrogen and oxygen with the $HfO_2$ layer during the rapid thermal annealing process, which results in the formation of a $TiO_x$/HfN interface layer, as schematically depicted in fig. 10 (a). The incorporation of nitrogen in the $HfO_2$ may, in turn, change the vacancy features at the interface as discussed by Baumgarten et al.[56].

### B. Interface stabilization

What happens at the TiN/$HfO_2$ bottom interface if additional oxygen is supplied before and during PVD growth, and what are the consequences for the defect distribution in $HfO_2$? From the previous results, we expect an interface exchange of oxygen and nitrogen dependent on the gradual increase of oxygen dosage.

In Fig. 12, the Ti 2p core level of samples prepared under different oxygen flows reveal contributions of several chemical species, namely TiN, $TiN_xO_y$ sub-oxides[57,58] and $TiO_2$. The increase of the oxygen flow during growth leads to a significant increase of the spectral weight of the $TiO_2$ component, starting from a small spectral weight at 0 sccm to a $\sim$ 1 : 1 ratio of $TiO_2$ and TiN for 2 sccm. From angular-dependent HAXPES measurements (not shown), it can be concluded that the $TiO_2$ contribution is located on top of the TiN bottom layer.

Since the $TiO_2$ peaks already appear for the amorphous $HfO_2$/TiN system (not shown) and thus are not related to the rapid thermal annealing crystallization process, an oxygen scavenging from $HfO_2$ can be excluded. Rather we conclude on the formation of a $TiO_2$ interlayer between the TiN bottom electrode and $HfO_2$. The $TiO_2$ interlayer thickness has been calculated from the $TiO_2$/TiN intensity ratio, taking into account the reduction of the TiN thickness at the expense of the $TiO_2$ growth (see ref.[53] for a detailed description). The resulting self-limiting layer growth is depicted in the inset of figure 12.

From the above HAXPES experiments, we propose the following chemical processes, which strongly determine the interface properties of TiN/$HfO_2$/TiN capacitors: The oxygen supply before $HfO_2$ growth generates a $TiO_2$ interface layer, which is self-limiting at about 3.5 nm. This layer effectively stabilizes the interface and prevents the exchange of oxygen and nitrogen. $TiO_2$ itself is chemically very stable and thus not expected to supply oxygen to the $HfO_2$ layer. Moreover, the interface stabilization by a $TiO_2$ buffer offers the possibility to design the defect properties of the atop $HfO_2$ layer deliberately by specific growth parameters.

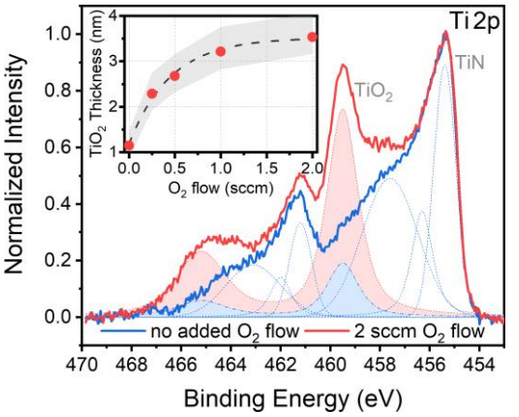


Figure 12. Ti 2p spectra recorded from the TiN bottom electrode of TiN/$HfO_2$-based MIM structures. A $TiO_2$ component appears with increasing oxygen supply before and during PVD growth of $HfO_2$ and signifies an interface oxide layer formation. The inset shows the oxygen flow-dependent thickness of this $TiO_2$ intralayer.

### C. Oxygen supply by $IrO_2$ electrodes

Finally, we explore the possibility of supplying oxygen into ferroelectric $HfO_2$ by an adjacent metal electrode. $IrO_2$ electrodes have been utilized as oxygen supplier in $IrO_2$/PZT/$IrO_2$ ferroelectric MIM structures[59]. Due to the resulting option to control the oxygen vacancy concentration in PZT, the ferroelectric performance of such MIM structure could be significantly optimized. The same effect was anticipated for $IrO_2$/Hf(Zr)$O_2$/$IrO_2$ MIM structures by increased controllability of HZO-related defects.

From the chemical perspective, $IrO_2$ readily supplies oxygen because it is an unstable compound and can be easily reduced to metallic Iridium at elevated temperatures[51]. Moreover, the choice of different annealing atmospheres has been found to crucially impact the $IrO_2$ composition and on the crystallization anneal process[60]. In figure 13, the Ir 4p and the O 1s core-levels are displayed. The Ir 4p emission around 495 eV shows different binding energies for annealing of

the $IrO_2$/Hf(Zr)$O_2$/$IrO_2$ in an oxygen atmosphere (OA) compared to forming gas annealing (FGA) (FG: 90% Ar, 10% $H_2$). The OA Ir $4p_{3/2}$ level appears at 800 meV higher binding energy, indicating a chemical shift. The $IrO_2$ top electrode is reduced to metallic Ir by the FG ambient, whereas the oxygen atmosphere, in turn, stabilizes the $IrO_2$ electrode. In addition, the metallic FGA Ir electrode shows an oxygen content at a binding energy of 533 eV, which is related to oxygen unbound to Ir (see inset)[60].

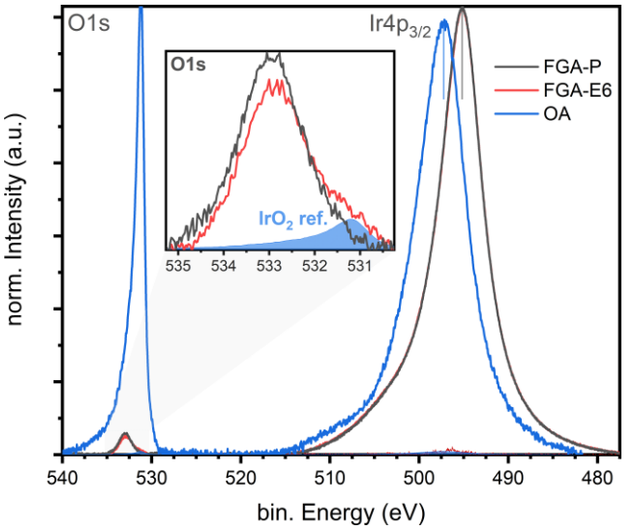


Figure 13. The Ir 4p and O 1s emission of the top electrode. The blue spectrum reflects the $IrO_2$ emission of the OA sample, whereas the black and red spectra reflect the chemically shifted emission from metallic Ir of the FGA samples. FGA-P and FGA-E6 are related to electrically untreated and $10^6$ times electrically cycled samples, respectively. The inset shows the O 1s emission of these two samples.

The emergence of metallic Ir electrodes containing unbound oxygen is of special interest to control the ferroelectric behaviour of the Ir/HZO interface during electrical switching of the MIM device. In the inset of figure 13, two spectra are displayed for which the FGA-annealed MIM device either had been electrically switched back and forth $10^6$ times (FGA-E6) or is electrically still untreated (FGA-P). A comparison reveals a modification of spectral weight in the O 1s component: The intensity of the unbound oxygen component at 533 eV decreases, while an additional component at 531 eV appears. This emission can be related to $IrO_2$. Thus, the application of the electrical switching pulses seemingly induces a chemical reaction at the interface. Such a reaction is most likely induced by charge injection into defect states at the interface. Whether this is accompanied by an oxygen migration across the interface can not be concluded from the current HAXPES results and requires further investigations.

The emergence of the $IrO_2$ component, as shown in figure 13 can be directly related to a changed band alignment at the interface. As discussed in section IV, binding energy shifts of core levels can be used as a measure of the binding energy shifts of the VB maximum relative to the Fermi level[13]. Here, the Hf 4f binding energy shift is used as a relative measure of the interfacial band alignment. Figure 14 shows the Hf 4f spectra of the OA and FGA samples, compared to samples annealed without top electrode (see Figure 14 (c)). From the Hf 4f binding energies of the samples without the top electrode, the band alignment at the bottom electrode is deducible. The $IrO_2$ top electrode of the OA sample shows a small shift of 130 meV towards lower binding energies (Figure 14 (b)), whereas the Ir top electrode of the electrically untreated FGA and FGA-P sample show a shift of 320 meV towards higher binding energies (Figure 14 (a)). After $10^6$ switching cycles (FGA-E6), however, the Hf 4f level has shifted back to the same binding energy as observed for the $IrO_2$ OA sample, see Figure 14 (b). This coincides with the appearance of the $IrO_2$ component at the interface and directly reflects the change from an Ir-related band alignment towards an $IrO_2$ related one. This shows the strong relation between interface chemistry and band alignment and again highlights the capability of HAXPES to address both.

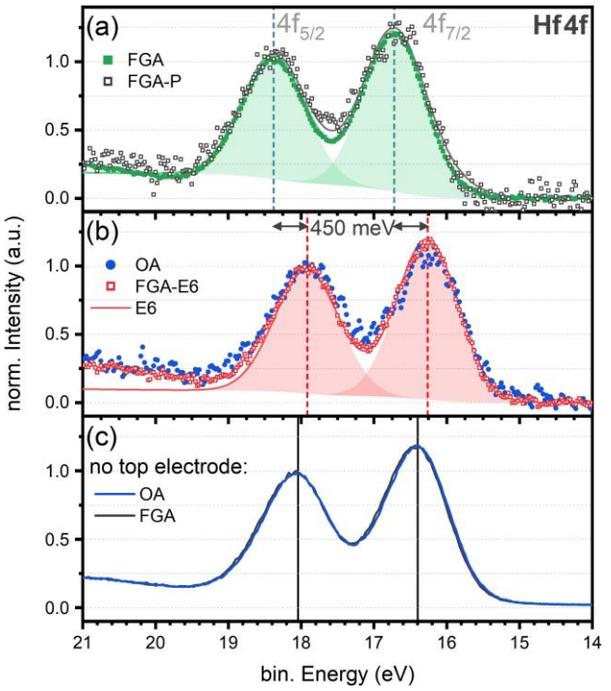


Figure 14. HAXPES spectra of the Hf 4f core levels for samples (a),(b) with top electrode under different annealing ambiences and cycling conditions, and (c) annealed without top electrode.

## VI. SUMMARY

In summary, oxide interfaces between (ultra-)thin films and substrates had been shown to offer exciting possibilities to set functionalities deliberately by a controlled oxygen exchange. The element-sensitivity of soft- and hard X-ray photoelectron spectroscopy allows to disentangle the specific mechanisms of how adjacent materials affect each other through, e.g., chemical reactions, ion diffusion or charge transfer, which may be related to electronic band bending or defect formation. In addition, the depth-sensitivity of HAXPES has been shown to be indispensable to probe these phenomena in a non-destructive manner at hidden interfaces and in real multilayer devices. In this regard, we presented spectroscopic results on emerging interface states and their tunability for selected ferro(i)magnetic and ferroelectric heterostructures – covering fundamental aspects and exploring application-relevant devices. The ability to tailor functional thin film properties will be key for future applications, e.g., in oxide electronics, which require full control over these complex electronic ground states.

## ACKNOWLEDGMENTS

The authors gratefully acknowledge beamtime support by Ch. Schlueter, A. Gloskovski, Y. Matveev, and W. Drube at the HAXPES beamline P22 (PETRA III, DESY Hamburg). Likewise, we wish to thank M. Gorgoi and R. F. Duarte for their support at the HIKE beamline (BESSY II, HZB Berlin).

The authors acknowledge DESY (Hamburg, Germany), a member of the Helmholtz Association HGF, for the provision of experimental facilities. Funding for the HAXPES instrument at beamline P22 by the Federal Ministry of Education and Research (BMBF) under contracts 05KS7UM1 and 05K10UMA with Universität Mainz and 05KS7WW3, 05K10WW1, and 05K13WW1 with Universität Würzburg is gratefully acknowledged.

We acknowledge R. Dittmann for providing the PLD setup at FZJ as well as O. Petracic and T. Brückel for providing measurement time at VSM at FZJ.

T.S., L.B. and M.M. acknowledge valuable discussions with U. Schroeder and T. Mittmann. Funding is acknowledged from the European Union's Horizon 2020 research and innovation programme under grant agreement No. 780302.

M.H.H. acknowledges support through a Tasso Springer Fellowship of the JCNS.

P.R. and M.M. acknowledge financial support by the Deutsche Forschungsgemeinschaft (DFG, German Research Foundation), International Collaborative Research Center No. TRR 160 (Project C9). M.M. acknowledges funding by DFG under SFB 1432 Project-ID 425217212.

M.M. wishes to express her gratitude to Chuck Fadley for being a mentor on her scientific path. In 2010, a joint beamtime using the first light of the former P09 (now P22) beamline at PETRA III opened the door towards HAXPES, and this journey is ever onward.

## DATA AVAILABILITY

The data that support the findings of this study are available from the corresponding author upon reasonable request.

## REFERENCES

[1] J. Mannhart and D. G. Schlom, "Oxide Interfaces – An Opportunity for Electronics," Science **327**, 1607 – 1611 (2010).
[2] H. Y. Hwang, Y. Iwasa, M. Kawasaki, B. Keimer, N. Nagaosa, and Y. Tokura, "Emergent phenomena at oxide interfaces," Nature Materials **11**, 103 – 113 (2012).
[3] M. Coll, J. Fontcuberta, M. Althammer, M. Bibes, H. Boschker, A. Calleja, G. Cheng, M. Cuoco, R. Dittmann, B. Dkhil, I. El Baggari, M. Fanciulli, I. Fina, E. Fortunato, C. Frontera, S. Fujita, V. Garcia, S. Goennenwein, C.-G. Granqvist, J. Grollier, R. Gross, A. Hagfeldt, G. Herranz, K. Hono, E. Houwman, M. Huijben, A. Kalaboukhov, D. Keeble, G. Koster, L. Kourkoutis, J. Levy, M. Lira-Cantu, J. MacManus-Driscoll, J. Mannhart, R. Martins, S. Menzel, T. Mikolajick, M. Napari, M. Nguyen, G. Niklasson, C. Paillard, S. Panigrahi, G. Rijnders, F. Sanchez, P. Sanchis, S. Sanna, D. Schlom, U. Schroeder, K. Shen, A. Siemon, M. Spreitzer, H. Sukegawa, R. Tamayo, J. van den Brink, N. Pryds, and F. M. Granozio, "Towards Oxide Electronics: a Roadmap," Applied Surface Science **482**, 1 – 93 (2019).
[4] C. Cancellieri and Strocov, Vladimir N., ***Spectroscopy of complex oxide interfaces*** (Springer Berlin Heidelberg, New York, NY, 2018).
[5] T. S. Böscke, J. Müller, D. Bräuhaus, U. Schröder, and U. Böttger, "Ferroelectricity in hafnium oxide thin films," Applied Physics Letters **99**, 102903 (2011), https://doi.org/10.1063/1.3634052.
[6] U. Schroeder, C. S. Hwang, and H. Funakubo, eds., ***Ferroelectricity in doped hafnium oxide: materials, properties and devices***, Woodhead Publishing series in electronic and optical materials (Woodhead Publishing, Duxford, United Kingdom, 2019).
[7] G. F. Dionne, ***Magnetic Oxides*** (Springer US, Boston, MA, 2009).
[8] A. Chouprik, D. Negrov, E. Y. Tsymbal, and A. Zenkevich, "Defects in ferroelectric $HfO_2$," Nanoscale , 10.1039.D1NR01260F (2021).
[9] C. S. Fadley, "Atomic-level characterization of materials with core- and valence-level photoemission: basic phenomena and future directions," Surface and Interface Analysis **40**, 1579 – 1605 (2008).
[10] C. Fadley, "X-ray photoelectron spectroscopy: Progress and perspectives," Journal of Electron Spectroscopy and Related Phenomena **178-179**, 2 – 32 (2010).
[11] J. Woicik, ed., ***Hard X-ray Photoelectron Spectroscopy (HAXPES)***, 1st ed., Springer Series in Surface Sciences No. 59 (Springer International Publishing : Imprint: Springer, Cham, 2016).
[12] M. Müller, S. Nemšák, L. Plucinski, and C. M. Schneider, "Functional materials for information and energy technology: Insights by photoelectron spectroscopy," Journal of Electron Spectroscopy and Related Phenomena **208**, 24 – 32 (2016), special Issue: Electronic structure and function from state-of-the-art spectroscopy and theory.

[13]E. A. Kraut, R. W. Grant, J. R. Waldrop, and S. P. Kowalczyk, "Precise determination of the valence-band edge in x-ray photoemission spectra: Application to measurement of semiconductor interface potentials," Physical Review Letters **44**, 1620 – 1623 (1980).

[14]P. G. Steeneken, L. H. Tjeng, I. Elfimov, G. A. Sawatzky, G. Ghiringhelli, N. B. Brookes, and D.-J. Huang, "Exchange Splitting and Charge Carrier Spin Polarization in EuO," Physical Review Letters **88**, 047201 (2002).

[15]G.-X. Miao, M. Müller, and J. S. Moodera, "Magnetoresistance in Double Spin Filter Tunnel Junctions with Nonmagnetic Electrodes and its Unconventional Bias Dependence," Physical Review Letters **102**, 076601 (2009).

[16]M. Müller, G.-X. Miao, and J. S. Moodera, "Exchange splitting and bias-dependent transport in EuO spin filter tunnel barriers," EPL (Europhysics Letters) **88**, 47006 (2009).

[17]P. Lömker, T. C. Rödel, T. Gerber, F. Fortuna, E. Frantzeskakis, P. Le Fèvre, F. Bertran, M. Müller, and A. F. Santander-Syro, "Two-dimensional electron system at the magnetically tunable EuO/SrTiO3 interface," Physical Review Materials, Rapid Communications **1**, 062001(R) (2017).

[18]K. J. Kormondy, L. Gao, X. Li, S. Lu, A. B. Posadas, S. Shen, M. Tsoi, M. R. McCartney, D. J. Smith, J. Zhou, L. L. Lev, M.-A. Husanu, V. N. Strocov, and A. A. Demkov, "Large positive linear magnetoresistance in the two-dimensional t 2g electron gas at the EuO/SrTiO3 interface," Scientific Reports **8**, 7721 (2018).

[19]P. Rosenberger, M. Opel, S. Geprägs, H. Huebl, R. Gross, M. Müller, and M. Althammer, "Quantifying the spin mixing conductance of euo/w heterostructures by spin hall magnetoresistance experiments," Applied Physics Letters **118**, 192401 (2021), https://doi.org/10.1063/5.0049235.

[20]V. Goian, R. Held, E. Bousquet, Y. Yuan, A. Melville, H. Zhou, V. Gopalan, P. Ghosez, N. A. Spaldin, D. G. Schlom, and S. Kamba, "Making EuO multiferroic by epitaxial strain engineering," Communications Materials **1**, 74 (2020).

[21]R. Sutarto, S. G. Altendorf, B. Coloru, M. Moretti Sala, T. Haupricht, C. F. Chang, Z. Hu, C. Schüßler-Langeheine, N. Hollmann, H. Kierspel, H. H. Hsieh, H.-J. Lin, C. T. Chen, and L. H. Tjeng, "Epitaxial and layer-by-layer growth of EuO thin films on yttria-stabilized cubic zirconia (001) using MBE distillation," Physical Review B **79** (2009), 10.1103/PhysRevB.79.205318.

[22]P. Lömker, "Interfacing EuOin confined oxide and metal heterostructures," Schriften des Forschungszentrums Jülich / Reihe Schlüsseltechnologien;174 (2018), 10.17877/DE290R-19124, publisher: Technische Universität Dortmund.

[23]T. Gerber, P. Lömker, B. Zijlstra, C. Besson, D. N. Mueller, W. Zander, J. Schubert, M. Gorgoi, and M. Müller, "Thermodynamic stability and control of oxygen reactivity at functional oxide interfaces: EuO on ITO," Journal of Materials Chemistry C **4**, 1813 – 1820 (2016).

[24]P. Rosenberger and M. Müller, "EuO/YSZ (001): The first monolayers under extreme distillation conditions," to be published (2021).

[25]M. Gorgoi, S. Svensson, F. Schäfers, G. Öhrwall, M. Mertin, P. Bressler, O. Karis, H. Siegbahn, A. Sandell, H. Rensmo, W. Doherty, C. Jung, W. Braun, and W. Eberhardt, "The high kinetic energy photoelectron spectroscopy facility at BESSY progress and first results," Nuclear Instruments and Methods in Physics Research Section A: Accelerators, Spectrometers, Detectors and Associated Equipment **601**, 48 – 53 (2009).

[26]H. Shinotsuka, S. Tanuma, C. J. Powell, and D. R. Penn, "Calculations of electron inelastic mean free paths. x. data for 41 elemental solids over the 50 eV to 200 keV range with the relativistic full penn algorithm: Calculations of electron inelastic mean free paths. x," Surface and Interface Analysis **47**, 871 – 888 (2015).

[27]J. F. Watts and J. Wolstenholme, ***An Introduction to Surface Analysis by XPS and AES*** (John Wiley & Sons, Ltd, 2003).

[28]P. Lömker and M. Müller, "Redox-controlled epitaxy and magnetism of oxide heterointerfaces: EuO / SrTiO 3," Physical Review Materials **3**, 061401 (2019).

[29]M. H. Hamed, ***Interface Functionalization of Magnetic Oxide $Fe_3O_4$/SrTiO$_3$ Heterostructures***, Dissertation, Univerität Duisburg, Jülich (2021), universität Duisburg, Diss., 2021.

[30]M. H. Hamed, R. A. Hinz, P. Lömker, M. Wilhelm, A. Gloskovskii, P. Bencok, C. Schmitz-Antoniak, H. Elnaggar, C. M. Schneider, and M. Müller, "Tunable magnetic phases at $Fe_3O_4$/SrTiO$_3$ oxide interfaces," ACS Applied Materials & Interfaces **11**, 7576 – 7583 (2019), https://doi.org/10.1021/acsami.8b20625.

[31]M. H. Hamed, D. N. Mueller, and M. Müller, "Active participation of "inert" YSZ substrates on interface formation in $Fe_3O_4$/YSZ heterostructures," Applied Surface Science Advances **6**, 100132 (2021).

[32]F. Walz, "The verwey transition - a topical review," Journal of Physics: Condensed Matter **14**, R285 – R340 (2002).

[33]H. Elnaggar, R. Wang, M. Ghiasi, M. Yañez, M. U. Delgado-Jaime, M. H. Hamed, A. Juhin, S. S. Dhesi, and F. de Groot, "Probing the local distortion of Fe sites in $Fe_3O_4$ thin films using enhanced symmetry selection in XMLD," Phys. Rev. Materials **4**, 024415 (2020).

[34]H. Elnaggar, M. W. Haverkort, M. H. Hamed, S. S. Dhesi, and F. M. F. de Groot, "Tensor description of X-ray magnetic dichroism at the Fe $L_2$, 3-edges of $Fe_3O_4$," Journal of Synchrotron Radiation **28**, 247 – 258 (2021).

[35]S. Gota, E. Guiot, M. Henriot, and M. Gautier-Soyer, "Atomic-oxygen-assisted MBE growth of $\alpha$-$Fe_2O_3$ on $\alpha$-$Al_2O_3$ (0001): Metastable FeO(111)-like phase at subnanometer thicknesses," Phys. Rev. B **60**, 14387 (1999).

[36]T. Fujii, F. M. F. de Groot, G. A. Sawatzky, F. C. Voogt, T. Hibma, and K. Okada, "In situ xps analysis of various iron oxide films grown by $NO_2$-assisted molecular-beam epitaxy," Phys. Rev. B **59**, 3195 (1999).

[37]A. Zenkevich, Y. Matveyev, M. Minnekaev, Y. Lebedinskii, S. Thiess, and W. Drube, "Electronic and electrical properties of functional interfaces studied by hard X-ray photoemission," Journal of Electron Spectroscopy and Related Phenomena **190**, 302 – 308 (2013).

[38]C. Lenser, A. Köhl, M. Patt, C. M. Schneider, R. Waser, and R. Dittmann, "Band alignment at memristive metal-oxide interfaces investigated by hard X-ray photoemission spectroscopy," Physical Review B **90**, 115312 (2014).

[39]M. Hoppe, S. Döring, M. Gorgoi, S. Cramm, and M. Müller, "Enhanced ferrimagnetism in auxetic $NiFe_2O_4$ in the crossover to the ultrathin-film limit," Physical Review B **91**, 054418 (2015).

[40]M. Hoppe, M. Gorgoi, C. M. Schneider, and M. Müller, "Wide-Range Structural and Chemical Stability of the Magnetic Oxide $NiFe_2O_4$ Grown by $O_2$-Assisted Pulsed Laser Deposition," IEEE Transactions on Magnetics **50**, 1 – 4 (2014).

[41]A. Gloskovskii, G. Stryganyuk, G. H. Fecher, C. Felser, S. Thiess, H. Schulz-Ritter, W. Drube, G. Berner, M. Sing, R. Claessen, and M. Yamamoto, "Magnetometry of buried layers—Linear magnetic dichroism and spin detection in angular resolved hard X-ray photoelectron spectroscopy," Journal of Electron Spectroscopy and Related Phenomena **185**, 47 – 52 (2012).

[42]H. Lüth, ***Surfaces and Interfaces of Solids***, 2nd ed., Springer Series in Surface Sciences, Vol. 15 (Springer Verlag Berlin Heidelberg, 1993) pp. 464 – 471.

[43]K. van Benthem, C. Elsässer, and R. H. French, "Bulk electronic structure of $SrTiO_3$: Experiment and theory," Journal of Applied Physics **90**, 6156 – 6164 (2001), https://doi.org/10.1063/1.1415766.

[44]K. Dileep, B. Loukya, N. Pachauri, A. Gupta, and R. Datta, "Probing optical band gaps at the nanoscale in $NiFe_2O_4$ and $CoFe_2O_4$ epitaxial films by high resolution electron energy loss spectroscopy," Journal of Applied Physics **116**, 103505 (2014), https://doi.org/10.1063/1.4895059.

[45]T. Mittmann, M. Materano, P. D. Lomenzo, M. H. Park, I. Stolichnov, M. Cavalieri, C. Zhou, C.-C. Chung, J. L. Jones, T. Szyjka, M. Müller, A. Kersch, T. Mikolajick, and U. Schroeder, "Origin of ferroelectric phase in undoped $HfO_2$ films deposited by sputtering," Adv.. Mater. Interfaces **6**, 1900042 (2019).

[46]H. Kohlstedt, Y. Mustafa, A. Gerber, A. Petraru, M. Fitsilis, R. Meyer, U. Böttger, and R. Waser, "Current status and challenges of ferroelectric memory devices," Microelectronic Engineering **80**, 296 – 304 (2005), 14th biennial Conference on Insulating Films on Semiconductors.

[47]F. P. G. Fengler, M. Pešić, S. Starschich, T. Schneller, U. Böttger, T. Schenk, M. H. Park, T. Mikolajick, and U. Schroeder, "Comparison of hafnia and pzt based ferroelectrics for future nonvolatile fram applications," in ***2016 46th European Solid-State Device Research Conference (ESSDERC)*** (2016) pp. 369 – 372.

[48]M. Pešić, F. P. G. Fengler, L. Larcher, A. Padovani, T. Schenk, E. D. Grimley, X. Sang, J. M. LeBeau, S. Slesazeck, U. Schroeder, and T. Mikolajick, "Physical mechanisms behind the field-cycling behavior of $HfO_2$-based ferroelectric capacitors," Advanced Functional Materials **26**, 4601 – 4612 (2016), https://onlinelibrary.wiley.com/doi/pdf/10.1002/adfm.201600590.

[49]C. Schlueter, A. Gloskovskii, K. Ederer, I. Schostak, S. Piec, I. Sarkar, Y. Matveyev, P. Lömker, M. Sing, R. Claessen, C. Wiemann, C. M. Schneider, K. Medjanik, G. Schönhense, P. Amann, A. Nilsson, W. Drube, S. Gwo, D.-J. Huang, and D.-H. Wei, "The new dedicated haxpes beamline P22 at PETRAIII," AIP Conference Proceedings **2054**, 040010 (2019), https://aip.scitation.org/doi/pdf/10.1063/1.5084611.

[50]J. C. Hackley and T. Gougousi, "Properties of atomic layer deposited $HfO_2$ thin films," Thin Solid Films **517**, 6576 – 6583 (2009).

[51]T. Mittmann, T. Szyjka, H. Alex, M. C. Istrate, P. D. Lomenzo, L. Baumgarten, M. Müller, J. L. Jones, L. Pintilie, T. Mikolajick, and U. Schroeder, "Impact of iridium oxide electrodes on the ferroelectric phase of thin $Hf_{0.5}Zr_{0.5}O_2$ films," physica status solidi (RRL) – Rapid Research Letters **n/a**, 2100012 (2021), https://onlinelibrary.wiley.com/doi/pdf/10.1002/pssr.202100012. [52]S. Suzer, S. Sayan, M. M. Banaszak Holl, E. Garfunkel, Z. Hus- sain, and N. M. Hamdan, "Soft x-ray photoemission studies of hf oxidation," Journal of Vacuum Science & Technology A **21**, 106 – 109 (2003), https://doi.org/10.1116/1.1525816.

[53]T. Szyjka, L. Baumgarten, T. Mittmann, Y. Matveyev, C. Schlueter, T. Mikolajick, U. Schroeder, and M. Müller, "Enhanced ferroelectric polarization in TiN/$HfO_2$/TiN capacitors by interface design," ACS Applied Electronic Materials **2**, 3152 – 3159 (2020), https://doi.org/10.1021/acsaelm.0c00503.

[54]M. Lee, Z.-H. Lu, W.-T. Ng, D. Landheer, X. Wu, and S. Moisa, "Interfacial growth in $HfO_xN_y$ gate dielectrics deposited using $[(C_2H_5)_2N]_4Hf$ with $O_2$ and NO," Applied Physics Letters **83**, 2638 – 2640 (2003), https://doi.org/10.1063/1.1608488.

[55]A. Glaser, S. Surnev, F. Netzer, N. Fateh, G. Fontalvo, and C. Mitterer, "Oxidation of vanadium nitride and titanium nitride coatings," Surface Science **601**, 1153 – 1159 (2007).

[56]L. Baumgarten, T. Szyjka, T. Mittmann, M. Materano, Y. Matveyev, C. Schlueter, T. Mikolajick, U. Schroeder, and M. Müller, "Impact of vacancies and impurities on ferroelectricity in PVD- and ALD-grown $HfO_2$ films," Applied Physics Letters **118**, 0 (2021), https://doi.org/10.1063/5.0035686.

[57]N. C. Saha and H. G. Tompkins, "Titanium nitride oxidation chemistry: An x-ray photoelectron spectroscopy study," Journal of Applied Physics **72**, 3072 – 3079 (1992), https://doi.org/10.1063/1.351465.

[58]C. Ernsberger, J. Nickerson, A. E. Miller, and J. Moulder, "Angular resolved x-ray photoelectron spectroscopy study of reactively sputtered titanium nitride," Journal of Vacuum Science & Technology A **3**, 2415 – 2418 (1985), https://doi.org/10.1116/1.572849.

[59]H. Fujisawa, S. Hyodo, K. Jitsui, M. Shimizu, H. Niu, H. Okino, and T. Shiosaki, "Electrical properties of pzt thin films grown on Ir/$IrO_2$ bottom electrodes by MOCVD," Integrated Ferroelectrics **21**, 107 – 114 (1998), https://doi.org/10.1080/10584589808202055.

[60]T. Szyjka, L. Baumgarten, T. Mittmann, Y. Matveyev, C. Schlueter, T. Mikolajick, U. Schroeder, and M. Müller, "Chemical stability of $IrO_2$ top electrodes in ferroelectric $Hf_{0.5}Zr_{0.5}O_2$-based metal – insulator – metal structures: The impact of annealing gas," physica status solidi (RRL) – Rapid Research Letters **n/a**, 2100027 (2021), https://onlinelibrary.wiley.com/doi/pdf/10.1002/pssr.202100027.

Journal of Vacuum Science Technology A


PLEASE CITE THIS ARTICLE AS DOI: 10.1116/6.0001491

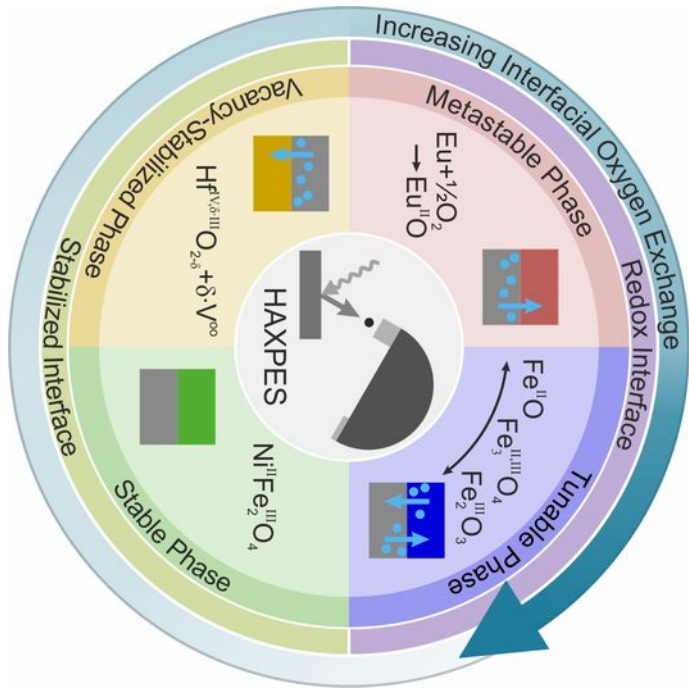

Journal of Vacuum Science Technology A

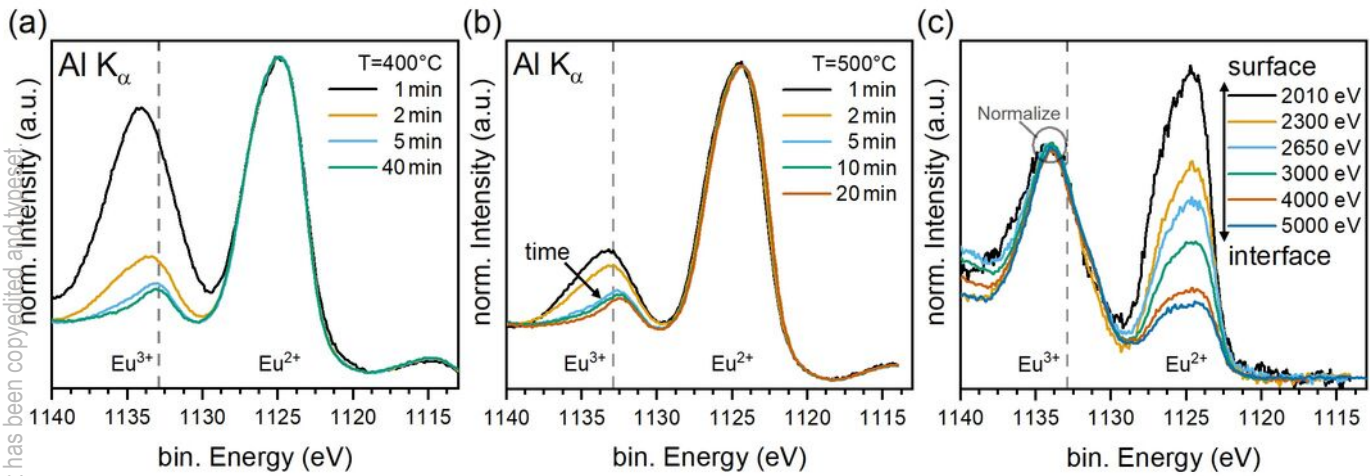

Journal of Vacuum Science Technology A



PLEASE CITE THIS ARTICLE AS DOI: 10.1116/6.0001491

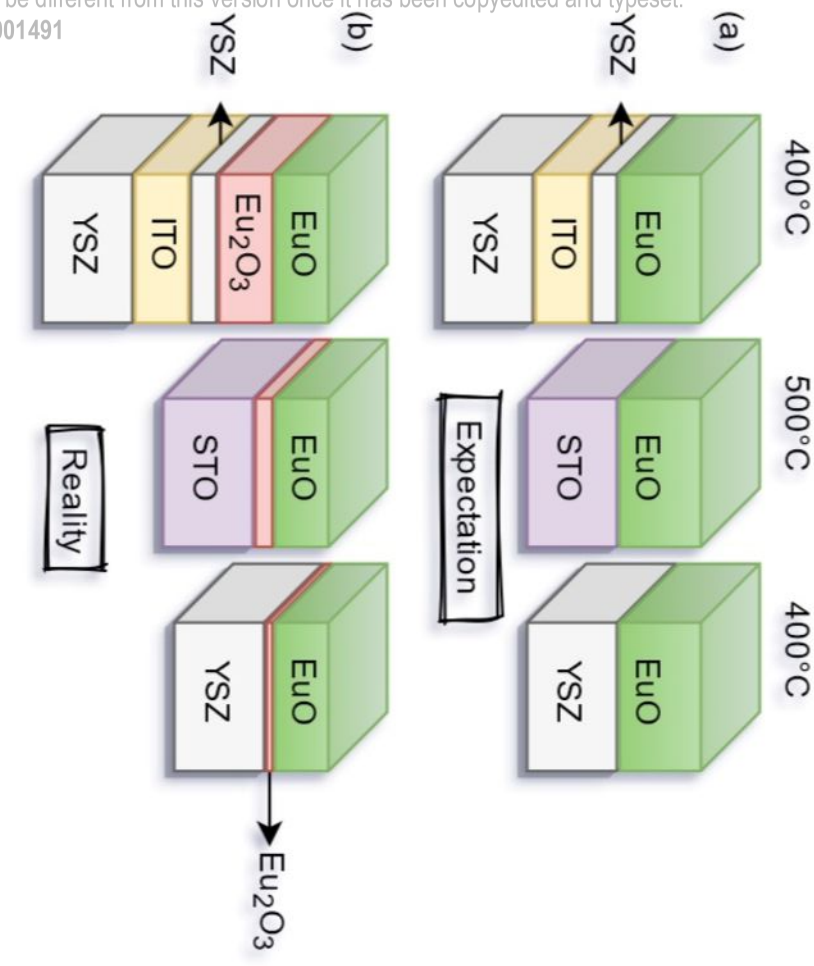

Journal of Vacuum Science Technology A


PLEASE CITE THIS ARTICLE AS DOI: 10.1116/6.0001491

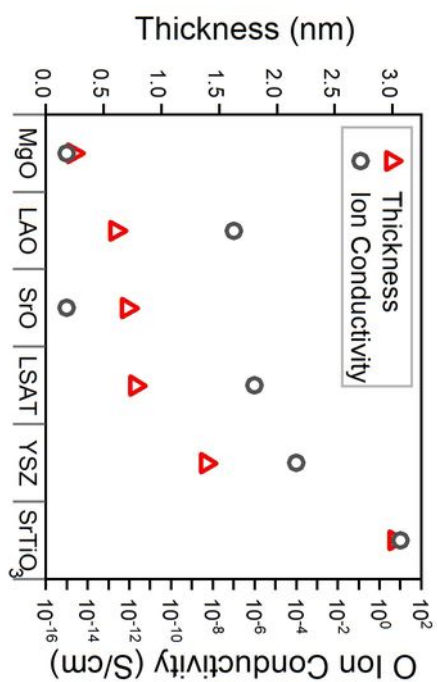

Journal of Vacuum Science Technology A



PLEASE CITE THIS ARTICLE AS DOI: 10.1116/6.0001491

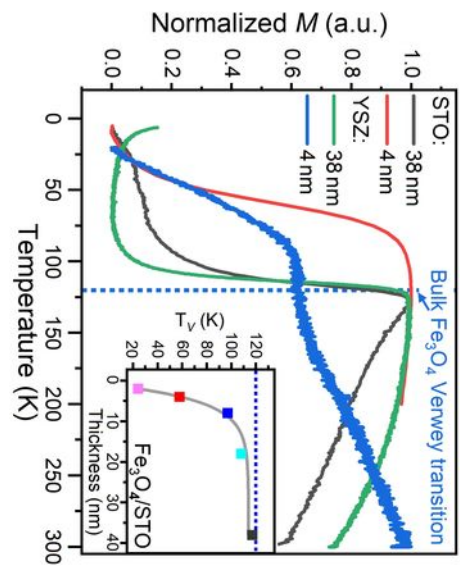

Journal of Vacuum Science Technology A

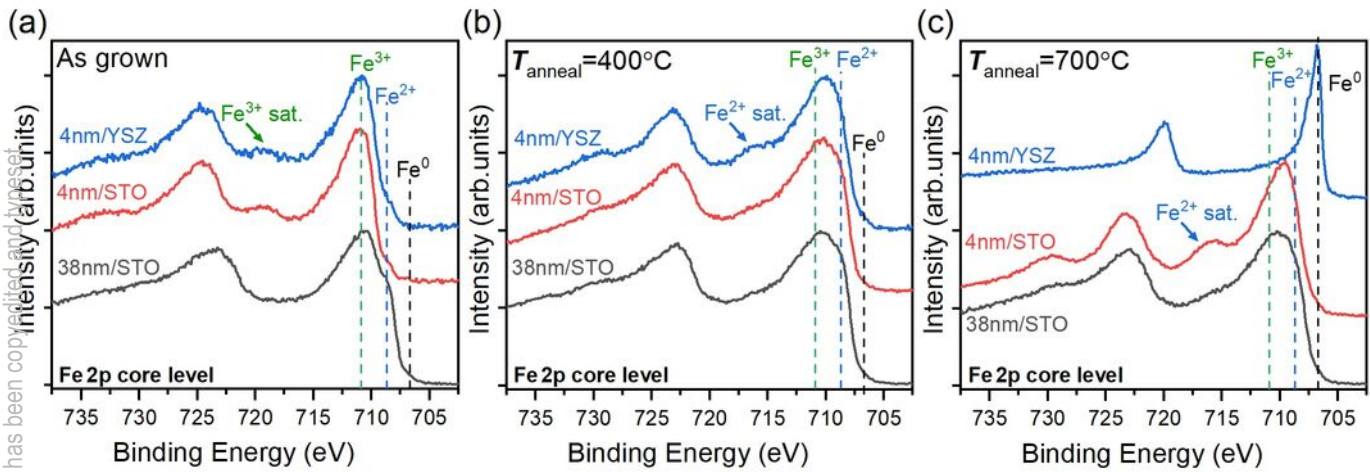




PLEASE CITE THIS ARTICLE AS DOI: 10.1116/6.0001491

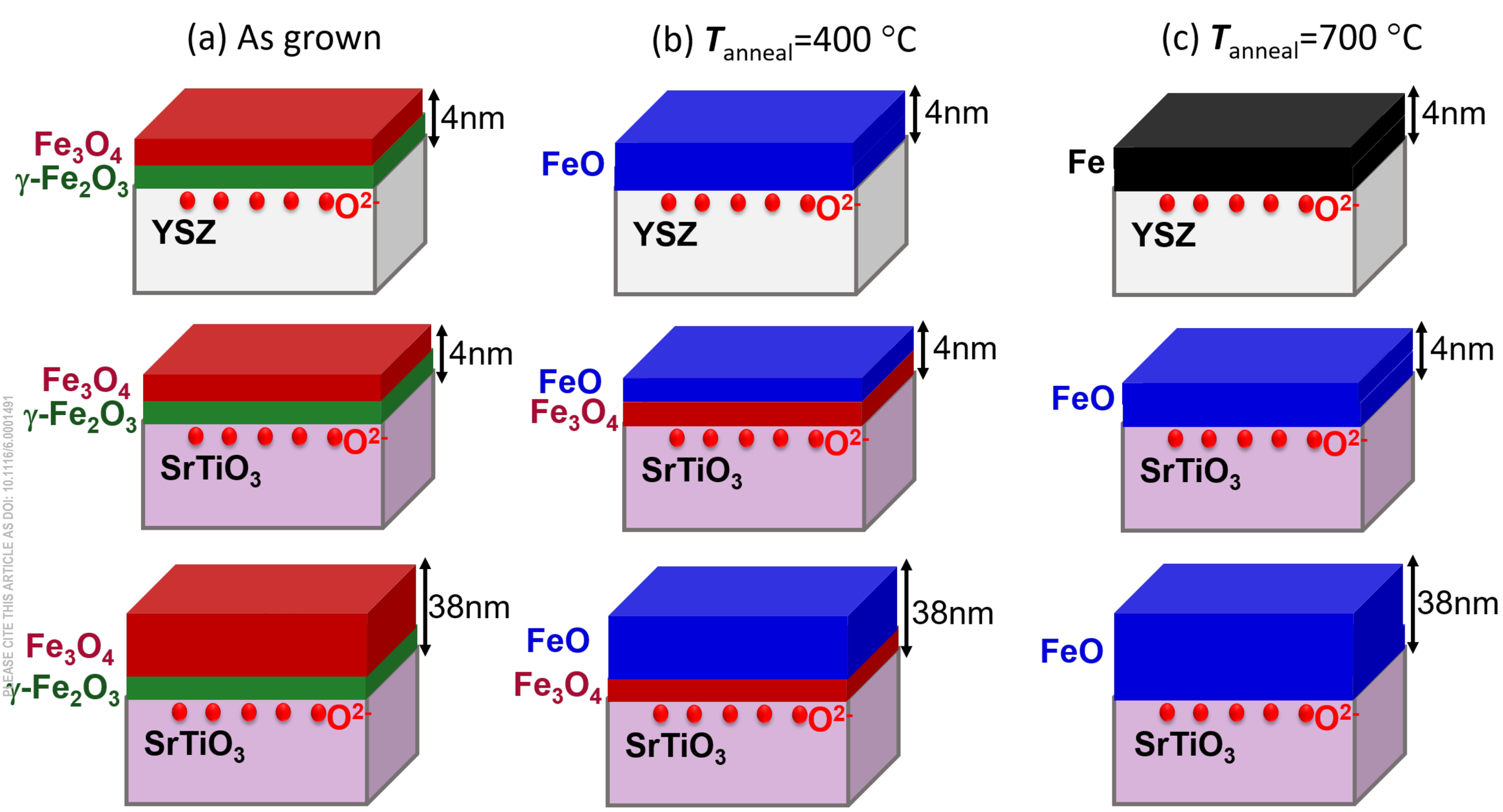

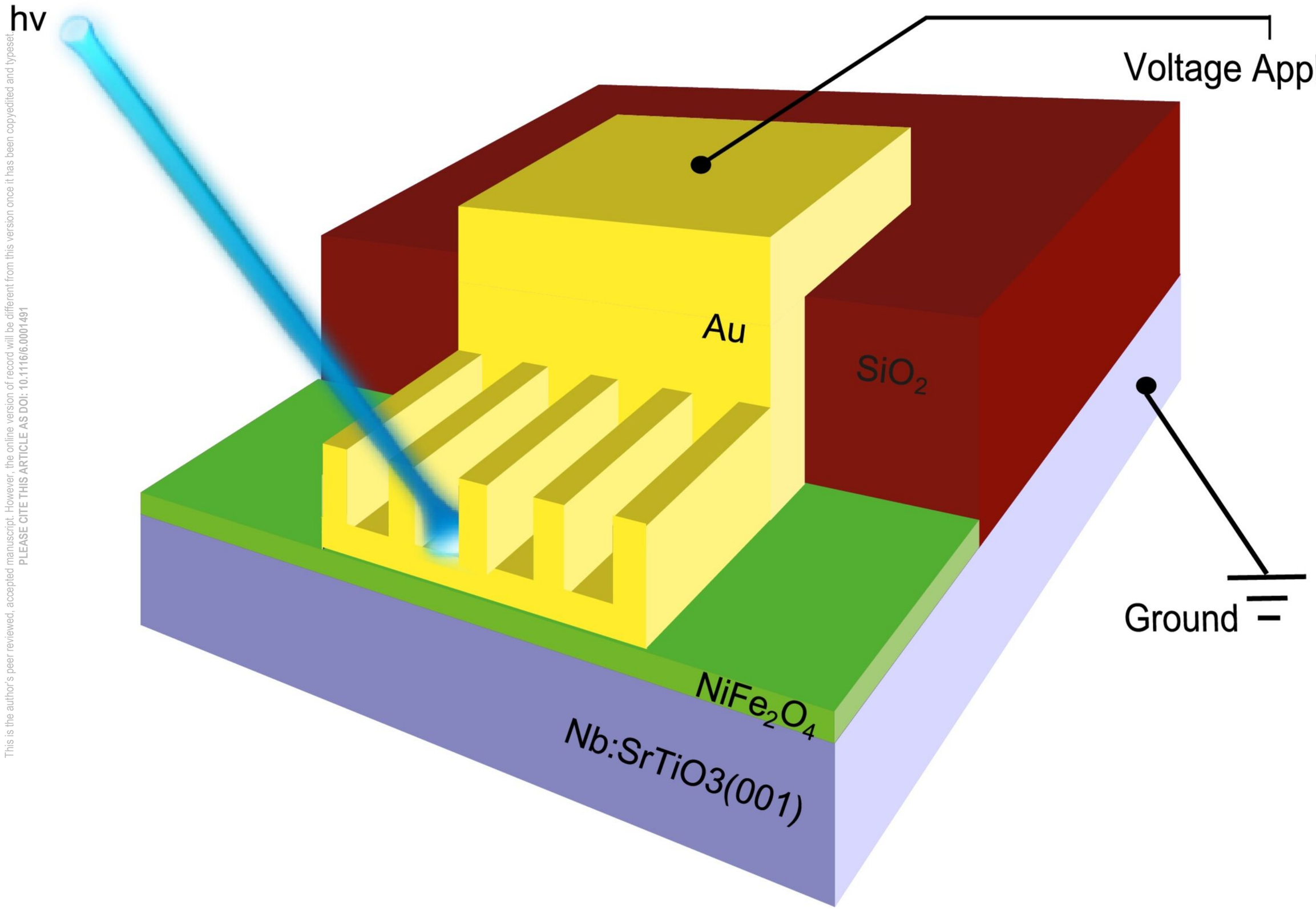

Journal of Vacuum Science Technology A



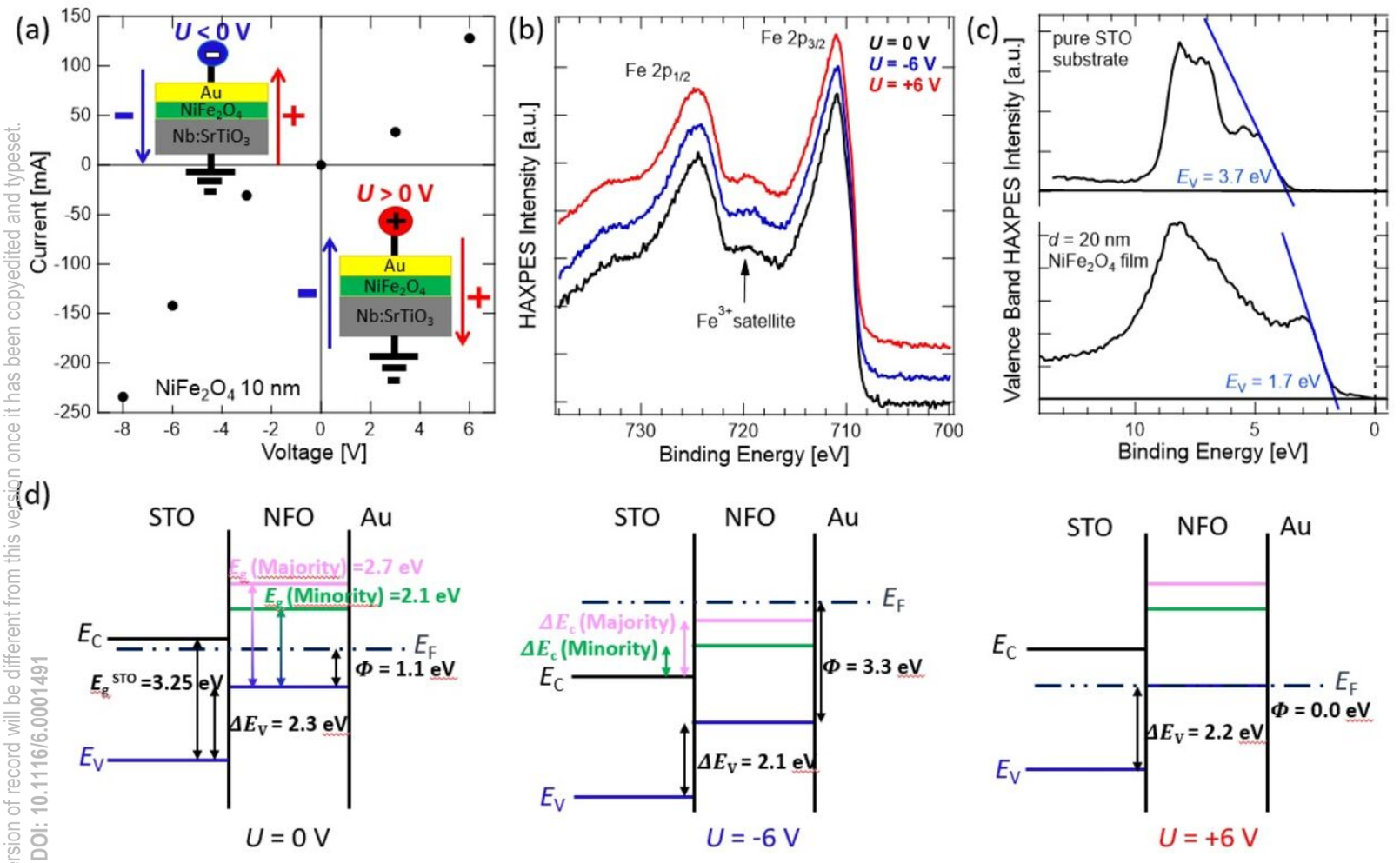

Journal of Vacuum Science Technology A



PLEASE CITE THIS ARTICLE AS DOI: 10.1116/6.0001491

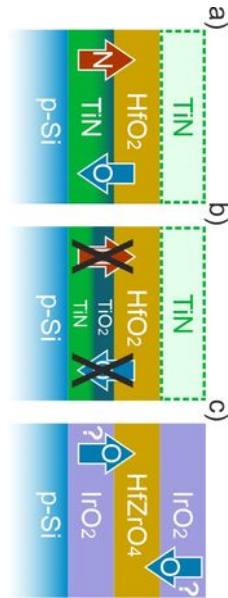

Journal of Vacuum Science Technology A


PLEASE CITE THIS ARTICLE AS DOI: 10.1116/6.0001491

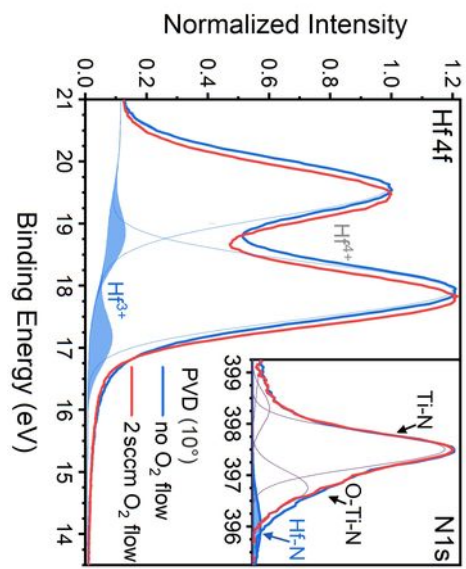

Journal of Vacuum Science Technology A



PLEASE CITE THIS ARTICLE AS DOI: 10.1116/6.0001491

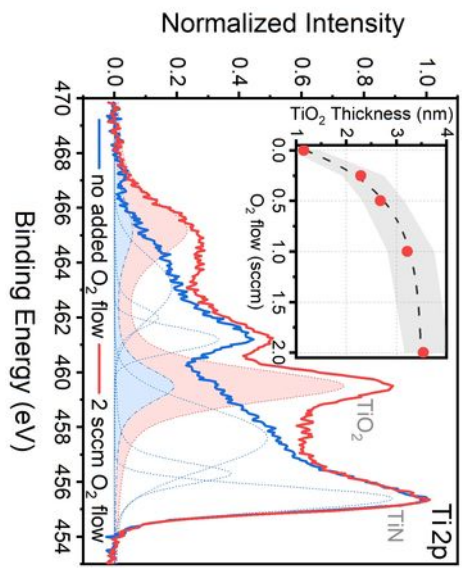

Journal of Vacuum Science Technology A



PLEASE CITE THIS ARTICLE AS DOI: 10.1116/6.0001491